~~Simulation characteristics~~Nonlinear Wavefield Characteristics of S~~s~~eismic T~~t~~ranslation and R~~r~~otation ~~under the nonlinearity~~ in S~~s~~mall-Strain D~~d~~eformation: Insights from Moment Tensor Simulations

Wei Li [1,2], Yun Wang [1,2,*], Chang Chen [1,2], Lixia Sun [1,3]

[1] *"MWMC" group, School of Geophysics and Information Technology, China University of Geosciences, Beijing* 100083, *China*

[2] *State Key Laboratory of Geological Processes and Mineral Resources, China University of Geosciences, Beijing* 100083, *China*

[3] *Sinopec Research Institute of Petroleum Engineering Co., Ltd., Beijing* 102206, *China*

[*] Corresponding author: wangyun@mail.gyig.ac.cn.

Abstract Seismic rotational motions recorded in near-field and strong-magnitude observations exhibit discrepancies with theoretical predictions derived from linear elastodynamic principles. To explore potential nonlinear contributions to the phenomenon, this study incorporates nonlinear strain effects into wave propagation theory through Green-Lagrange strain tensor formulations. A staggered-grid finite-difference method simulates six-component wavefields (translational and rotational) generated by three fundamental seismic sources: isotropic (ISO), double-couple (DC), and compensated linear vector dipole (CLVD). Results demonstrate that nonlinear effects strongly depend on source characteristics and

energy intensity. ISO sources exhibit uniform nonlinear anomalies from volumetric-shear coupling, CLVD sources amplify directional strain-axis effects, and DC sources amplify localized nonlinearity along faulting directions. Rotational components show higher sensitivity to nonlinearity than translational components, which are also contingent on source-receiver geometry. Simulations of two moderate-strong earthquakes highlight surface waves as preferential carriers of nonlinear signatures, though path effects and site amplification require systematic exploration. These results establish a framework for advancing nonlinearity study in ground motion analysis while emphasizing the need for instrumentally resolved rotational measurements and complex media modeling.

~~Ground motions consist of three translational motions along orthogonal axes and three rotational motions around the axes. Recording all six seismic components facilitates obtaining comprehensive vector wavefield information and restoring complete ground displacement. Classical elastic dynamics of elastic wave propagation assume linearity in small deformations of medium particles. However, seismic rotational observations reveal significant discrepancies between the directly recorded rotational motions in the near field and those derived from calculations based on the traditional theory. Considering that nonlinear effects might be pivotal in contributing to this discrepancy, this study incorporates the previously neglected nonlinearity in small deformation into elastodynamic principles to derive velocity-stress elastic wave equations and apply the staggered-grid finite-difference method to simulate the propagation of seismic waves. The staggered-grid finite-difference method is then employed to simulate the~~

~~propagation of seismic waves. Simulations were conducted for the translational and rotational components induced by isotropic (ISO), double couple (DC), and compensated linear vector dipole (CLVD) sources the three fundamental seismic source types described by moment tensor. These simulations allowed for a comparison of the influence of nonlinearity on wavefield anomalies. The results indicate that the error associated with linear approximation is more pronounced in ISO and CLVD source simulations. The nonlinear effect exhibits a greater impact on rotational motions than translational components, particularly in strong earthquakes. We simulated two actual seismicities Taiwan and compared the synthetic records under linear and nonlinear models. Further explorations are still needed to investigate the specific influence of complex propagation path properties and seismic source mechanisms on nonlinear effects.~~

1 Introduction

Seismic rotational motions can be recorded in ground shaking, especially when caused by strong earthquakes (Graizer, 1991; 2010; Zhou et al., 2019). These rotational motions exhibit pronounced characteristics~~induced by strong earthquakes is particularly prominent~~ in shallow ~~foci~~ focal depths and near-field conditions (Kozak, 2009; Sun et al., 2017). Within the domain~~In the field~~ of structural ~~architecture~~ engineering, the incorporation of rotational analysis has gained increasing recognition for its critical role~~is encouraged to be considered~~ in assessing ~~the stability of~~ ground motion~~s~~ stability and building design (Li, 1991; Li and Sun, 2001; Yan, 2017; Huras et al., 2021). S~~everal s~~tudies advancements suggest that incorporating seismic rotation data, which captures spatial gradients, can enhance the ~~precision~~ accuracy of earthquake source characterization ~~prediction~~ and moment tensor inversion (Bernauer et al., 2014; Donner, 2016; Ichinose et al., 2021), as supported by simulations conducted by Hua and Zhang (2022).

The work of Lee (2007) comprehensively reviewed the ~~summarized~~ applications of ~~observing~~ seismic rotation~~s~~ observations i~~o~~n seismic engineering, postulating ~~and inferred~~ that the measured ~~seismic~~ rotation~~s~~ components in strong ground motion are predominantly ~~should mainly~~originate from the nonlinear elasticity and site effect~~,~~. This conclusion is drawn from empirical evidence showing that actual rotational measurements exceed derived rotational components from translational data by~~since the real rotational components measured in strong ground motion are greater~~ 1-2 orders ~~than the derived ones from translational components~~of magnitude. ~~Recognizing~~

~~the pivotal role of nonlinear waves~~ I~~i~~n addressing the complex geophysical phenomena ~~complexities~~ stemming from Earth's heterogeneities, progress has been made in developing ~~various~~ analytical solutions ~~of~~ for nonlinear wave equations ~~have been developed~~ through iterative techniques in Green's function (McCall, 1994). Notable methodological developments~~These~~ include the flux-corrected transport method (Yang et al., 2002; Zheng et al., 2006) and perturbation approaches (Bataille and Contreras, 2009; Jia et al., 2020), which have been instrumental ~~to~~ in investigating~~e~~ ~~the~~ nonlinear effects on elastic wave propagation~~s~~. However, ~~most~~ current studies primarily focus on ~~the~~ nonlinear constitutive relations between stress and strain~~, based on~~ under small ~~deformation~~ strain and its linearization approximations ~~assumption~~ (Renaud et al., 2012; 2013; TenCate et al., 2016; Feng et al., 2018~~).~~), leaving a gap in understanding ~~There is a scarcity of exploration into~~ the strain nonlinearity ~~of deformations,~~. This aspect ~~which~~ may hold the key to~~represent a crucial aspect for~~ more accurate representations of~~better approximating~~ rotational motions ~~of~~ in strong earthquakes and near-field conditions.

In the seismically active region of Taiwan, ~~situated in an active seismic zone,~~ broadband seismic observations and ~~studies of~~ physical source studies ~~of seismic sources~~ have revealed ~~presented~~ significant~~that there are non-ignorable~~ rotational components ~~motions~~ in Taiwan's seismic events, ~~earthquakes~~ demonstrating~~and showed~~ distinct ~~different~~ strike-slip rotation characteristics between ~~in~~ the southern and northern regions of the island (Yu et al., 1999; Wang and Lv, 2006). Oliveira and Bolt (1989) estimated rotational components of strong motions, confirming their~~and~~

~~verified that the rotation effect could not be~~ non-negligible impact~~ected~~ in near-field observations across ~~on~~ Taiwan~~ Island~~. Through analysis of~~Using measured~~ six-component ground motion data ~~of~~ from 52 earthquakes recorded ~~during 2007-2008~~ at the HGSD station in eastern Taiwan during 2007-2008, Chen et al. (2014) identified substantial~~pointed out the existence of large~~ vertical rotational motions ~~at~~ in proximal ~~near~~ seismic locations and notable ~~significant~~ differences in energy and spectral characteristics between ~~of~~ horizontal and vertical rotational motions. These studies show the importance of seismic rotation analysis in elucidating Taiwan's subsurface structures and geodynamic~~s~~ processes.

In this research, we develop a theoretical and numerical framework for analyzing nonlinear seismic wave propagation through Green strain tensor formulations. We derive ~~the~~ velocity-stress~~nonlinear wave~~ equations incorporating nonlinear strain coupling terms, employ a staggered-grid finite-difference method to simulate six-component wavefields, and examine ~~discuss the~~ nonlinear six-component (~~6~~C) ~~rotation~~ wavefield characteristics ~~under the nonlinearity in small deformation condition~~ through numerical simulations of three fundamental seismic moment tensor sources. Additionally~~Furthermore~~, we conduct~~engage in~~ theoretical simulations of focal mechanisms of ~~six-component (~~near-field and strong~~6C) wavefields of for both a near-field and a strong~~ ~~seismicities~~ earthquakes ~~seismic events~~ along the ~~in~~ Taiwan coast, ~~to discuss~~ analyzing ~~compare~~ source-dependent nonlinear responses to establish foundational insights for guiding future observational data studies~~the effects of nonlinearity in seismic wave propagation~~.

2 Theory and method

2.1 Elastodynamic theory

Consider an elastic medium i~~I~~n ~~a~~ three-dimensional space under orthogonal Cartesian coordinate~~–~~ (Fig. 1)~~system, an elastic body within elastic space, as illustrated in Fig.~~ . Let~~1,~~ particle ~~point~~ A at position **x** within the ~~elastic~~ medium~~body is denoted as **x**~~, with~~.~~ an adjacent particle ~~Point~~ B at~~is adjacent to the point A, indicated as~~ **x**+d**x**. The infinitesimal line element connecting these particles has an initial length~~distance separating A and B is defined as~~ ds. When subjected to~~Upon instantaneous motivation of an~~ external force, the material~~elastic mass~~ element AB undergoes ~~a~~ displacement $\boldsymbol{u}(\boldsymbol{x}, t)$, transitioning to ~~a~~ new positions A' and B' at **x**' and **x**'+d**x**', respectively, with a deformed length ds'~~location A'B'~~. This deformation ~~displacement~~ comprises~~is characterized by~~ both rigid-body displacement and strain-induced distortion~~accompanied by small deformation of the elastic body, where the new positions of A' and B' are designated as **x**' and **x**'+d**x**', respectively, with their distance denoted as ds'~~. The work performed ~~done~~ by the external force ~~i~~manifests as~~s primarily converted into~~ kinetic energy from particle motion~~due to the displacement~~ and potential energy stored through~~stemming from the~~ elastic deformation. The strain energy density ~~deformation is~~can be quantified by the differential quadratic form of the line element's length variation~~change in the square of the length of the line element before and after deformation, i.e., the squared difference in distance between~~

~~AB and A'B', which is mathematically~~ given in~~expressed through~~ Eq. (1). ~~The following equations and tensors are written using dummy index notation rules.~~

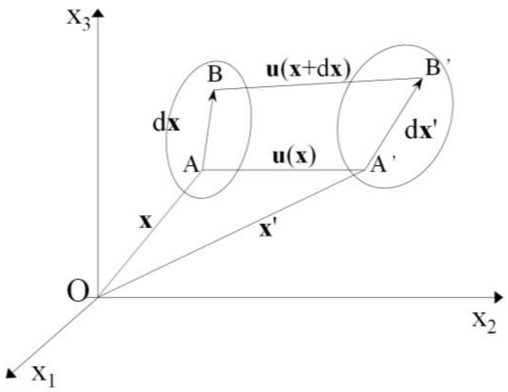

Figure 1. Schematic diagram of displacement and deformation of an ~~an~~ elast~~omer~~ic medium (Adapted from Aki and Richards (2002))

$$(ds')^2-(ds)^2 = 2E_{ij}dx_i dx_j,\ i, j \in \{1,2,3\} \qquad (1)$$

where E_{ij} denotes the Green-Lagrange strain tensor components. All tensor equations adhere to the Einstein summation convention with dummy index notation. The displacement field u_i~~i~~ ~~and u_j are the displacements along different directions, and x_i and x_j are the~~in Cartesian coordinate x_j~~s.~~ defines the~~Therefore,~~ Green strain tensor ~~(E_{ij}, given by~~ Eq. (2)~~),)~~)~~. The Green strain tensor is~~, which provides an objective measure of deformation before and after ~~applying~~ external force ~~to an elastomer.~~application~~is an objective measure of deformation before and after applying external force to an elastomer.~~

$$E_{ij} = \frac{1}{2}\left(\frac{\partial u_j}{\partial x_i} + \frac{\partial u_i}{\partial x_j} + \frac{\partial u_k}{\partial x_i}\cdot\frac{\partial u_k}{\partial x_j}\right),\ i, j, k \in \{1,2,3\} \qquad (2)$$

The displacement gradient tensor decomposes into symmetric~~Within the elastodynamic theory,~~ strain (e_{ij}) and antisymmetric rotation (r_{ij}) components~~tensors are defined as follows~~:

$$\frac{\partial u_j}{\partial x_i} = e_{ij} + r_{ij} \tag{3}$$

$$e_{ij} = \frac{1}{2}\left(\frac{\partial u_j}{\partial x_i} + \frac{\partial u_i}{\partial x_j}\right), \quad r_{ij} = \frac{1}{2}\left(\frac{\partial u_i}{\partial x_j} - \frac{\partial u_j}{\partial x_i}\right) \tag{4}$$

Conventional elastodynamic theory linearizes the Green strain tensor by neglecting second-order displacement gradient terms ($\partial u_k/x_i\, \partial u_k/x_{j\cancel{i}}$), reducing it to the infinitesimal strain approximation:~~Based on Eqs. (3) and (4), the Green strain tensor can also be written as Eq. (5).~~

$$E_{ij} \approx e_{ij} = \frac{1}{2}\left(\frac{\partial u_j}{\partial x_i} + \frac{\partial u_i}{\partial x_j}\right), \; i, j \in \{1, 2, 3\} \tag{5}$$

~~The second-order nonlinear displacements in Eq. (2) are neglected in the classical elastodynamic theory, which focuses on the first-order linear terms and neglecting the second-order terms of the strain tensor and the rotation tensor in Eq. (5), thereby reducing the Green strain tensor to its linear approximation e_{ij}.~~

~~In~~For isotropic elastic materials, the ~~relationship between~~ strain-~~- and~~ stress relationship is given by~~used to characterize an elastomer is~~:

$$\sigma_{ij} = \lambda \delta_{ij} e_{kk} + 2\mu e_{ij}, \; i, j, k \in \{1, 2, 3\} \tag{6}$$

where λ and μ are Lamé coefficients, and δ_{ij} is the Kronecker delta~~symbol~~. Incorporating nonlinearity through the complete Green strain tensor yields:

$$\begin{aligned}\sigma_{ij} &= \lambda \delta_{ij} E_{kk} + 2\mu E_{ij} \\ &= \lambda \delta_{ij} e_{kk} + 2\mu e_{ij} + \underbrace{\frac{1}{2}\lambda \delta_{ij}\left(\frac{\partial u_k}{\partial x_m} \cdot \frac{\partial u_k}{\partial x_m}\right) + \mu \frac{\partial u_k}{\partial x_i} \cdot \frac{\partial u_k}{\partial x_j}}_{\text{additional terms}}, \; i, j, k, m \in \{1, 2, 3\}\end{aligned} \tag{7}$$

S~~Then, s~~ubstituting ~~Eq. (7)~~ the~~containing~~ nonlinear constitutive relation (Eq. (7))~~contributions~~ into the momentum conservation law (Eq. (8)), ~~representing the~~

~~stress-strain relationship yields Eq. (9),~~ where ρ is the material density.

$$\rho \frac{\partial^2 u_i}{\partial t^2} = \frac{\partial \sigma_{ij}}{\partial x_j},\ i, j \in \{1,2,3\} \tag{8}$$

Yields the nonlinear wave equation:

$$\begin{aligned}\rho \frac{\partial^2 u_i}{\partial t^2} &= \frac{\partial}{\partial x_j}\left(\lambda \delta_{ij} E_{kk} + 2\mu E_{ij}\right) \\ &= \underbrace{(\lambda+\mu)\frac{\partial^2 u_j}{\partial x_i \partial x_j} + \mu \frac{\partial^2 u_i}{\partial x_j \partial x_j}}_{\text{original terms}} + \underbrace{\lambda \frac{\partial u_k}{\partial x_i}\frac{\partial^2 u_k}{\partial x_j x_j} + \mu\left(\frac{\partial^2 u_k}{\partial x_i x_j}\frac{\partial u_k}{\partial x_j} + \frac{\partial^2 u_k}{\partial x_j x_j}\frac{\partial u_k}{\partial x_i}\right)}_{\text{additional terms}},\ i, j, k \in \{1,2,3\}\end{aligned}$$

~~i, j, k∈{1,2,3}~~ (9)

In Eq. (9), the ~~first two terms on the right side of the equal sign~~original terms correspond to ~~are the results of~~ the classical linear wave equation ~~under the linear strain tensor~~, while ~~and~~ the ~~last two terms~~additional terms ~~are the increased terms in the wave equation~~arise from~~emerge after~~ the nonlinear strain contributions ~~is applied~~. ~~Eq. (9)~~This ~~shows the difference in equation expression between using the linear and nonlinear strains.~~

~~Equation (9)~~ reveals two fundamental nonlinear effects: (i) Volumetric nonlinearity (associated with λ): Coupling between shear deformation and volumetric strain. (ii) Shear nonlinearity (associated with μ): Interdependence of shear stress and principal strains. ~~Compared to the original equation which contains only the first two terms of the right of the equal sign in~~These ~~Eq. (9). The nonlinearity introduces~~ additional ~~several~~ third-order terms introduce ~~that add more physical~~ complex~~ity~~ ~~v~~interactions between deformation modes that are absent in linear theory~~ia material's elastic property~~. ~~The part associated with the bulk modulus λ reflects that the volumetric deformation is no longer limited to the original purely linear principal~~

~~strains but also the volumetric change induced by shear deformation, which is an important feature of the material's nonlinear elastic behavior. The part related to the shear modulus μ additionally describes the shear deformation property. The elastic shear deformation is not merely a direct consequence of shear stress but also exhibits a correlation with the principal strains shown in Eq. (9).~~ Their seismic manifestations depend critically on material properties and source characteristics, necessitating targeted numerical simulations to quantify nonlinear effects on wave propagation. ~~The additional terms in Eq. (9) do not directly correspond to the wavefield difference, and in earthquakes, their manifestation may vary depending on the material properties and source loading. Therefore, it is necessary to assess the effect of the material's nonlinear elasticity on seismic wave propagation by specific theoretical numerical simulations.~~

2.2 Staggered-grid finite-difference ~~simulation~~ method

The staggered-grid finite-difference (SGFD) technique ~~method~~ has proven effective~~been a technique~~ for simulating ~~numerical simulations of~~ seismic wave propagation~~fields~~. ~~In~~ T~~t~~his method~~, the medium is divided into two~~ employs dual grid systems ~~and~~ to discretize velocity-stress formulations~~wave equations~~, enabling~~are discretized in these grids, thereby allowing~~ stable computation~~ng~~ ~~the~~ of ~~numerical solution of~~ wavefield evolution~~s~~ ~~across~~in ~~at~~ discrete spatial~~ and ~~-temporal domains~~each grid point as time progresses~~ (Madariaga, 1976; Sun et al., 2018). As illustrated in Fig~~ure~~. 2~~, illustrates~~~~For example, the grid configuration for a two~~three~~-dimensional (3D)~~ ~~staggered-grid configuration where~~ stress and velocity components are distributed across offset grid points to optimize numerical accuracy.~~scenario is shown in Fig. 2.~~

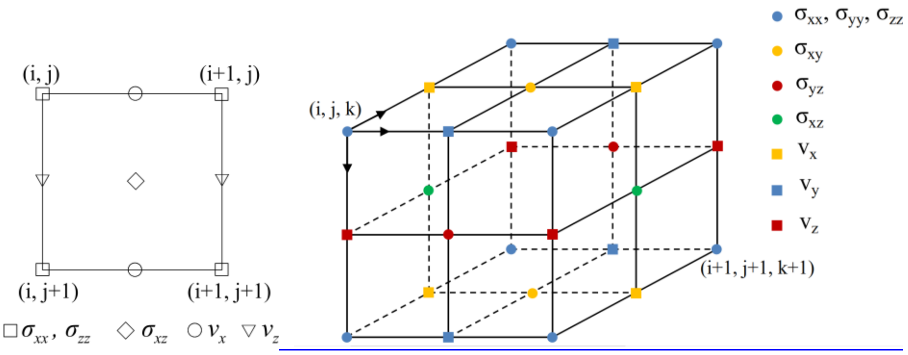

Figure 2. 3D staggered-grid configuration for velocity-stress formulations.~~Schematic diagram of 2D staggered grids~~

For ~~three-dimensional~~ 3D~~(3D)~~ elastic isotropic media, we extend ~~using~~ conventional linear strain formulations (Pei, 2005~~).~~) by incorporating ~~Firstly, the individual stress components using~~ the nonlinear strain tensor E_{ij} ~~are givern in Eq. (10).~~:

$$
\begin{aligned}
\sigma_{xx} &= \lambda\left\{\frac{\partial u_x}{\partial x}+\frac{\partial u_y}{\partial y}+\frac{\partial u_z}{\partial z}+\frac{1}{2}\left[(\frac{\partial u_x}{\partial x})^2+(\frac{\partial u_y}{\partial x})^2+(\frac{\partial u_z}{\partial x})^2+(\frac{\partial u_x}{\partial y})^2+(\frac{\partial u_y}{\partial y})^2+(\frac{\partial u_z}{\partial y})^2+(\frac{\partial u_x}{\partial z})^2+(\frac{\partial u_y}{\partial z})^2+(\frac{\partial u_z}{\partial z})^2\right]\right\}\\
&\quad+\mu\left[\frac{\partial u_x}{\partial x}+(\frac{\partial u_x}{\partial x})^2+(\frac{\partial u_y}{\partial x})^2+(\frac{\partial u_z}{\partial x})^2\right]\\
\sigma_{yy} &= \lambda\left\{\frac{\partial u_x}{\partial x}+\frac{\partial u_y}{\partial y}+\frac{\partial u_z}{\partial z}+\frac{1}{2}\left[(\frac{\partial u_x}{\partial x})^2+(\frac{\partial u_y}{\partial x})^2+(\frac{\partial u_z}{\partial x})^2+(\frac{\partial u_x}{\partial y})^2+(\frac{\partial u_y}{\partial y})^2+(\frac{\partial u_z}{\partial y})^2+(\frac{\partial u_x}{\partial z})^2+(\frac{\partial u_y}{\partial z})^2+(\frac{\partial u_z}{\partial z})^2\right]\right\}\\
&\quad+\mu\left[\frac{\partial u_y}{\partial y}+(\frac{\partial u_x}{\partial y})^2+(\frac{\partial u_y}{\partial y})^2+(\frac{\partial u_z}{\partial y})^2\right]\\
\sigma_{zz} &= \lambda\left\{\frac{\partial u_x}{\partial x}+\frac{\partial u_y}{\partial y}+\frac{\partial u_z}{\partial z}+\frac{1}{2}\left[(\frac{\partial u_x}{\partial x})^2+(\frac{\partial u_y}{\partial x})^2+(\frac{\partial u_z}{\partial x})^2+(\frac{\partial u_x}{\partial y})^2+(\frac{\partial u_y}{\partial y})^2+(\frac{\partial u_z}{\partial y})^2+(\frac{\partial u_x}{\partial z})^2+(\frac{\partial u_y}{\partial z})^2+(\frac{\partial u_z}{\partial z})^2\right]\right\}\\
&\quad+\mu\left[\frac{\partial u_z}{\partial z}+(\frac{\partial u_x}{\partial z})^2+(\frac{\partial u_y}{\partial z})^2+(\frac{\partial u_z}{\partial z})^2\right]\\
\sigma_{xy} &= \sigma_{yx} = \mu\left(\frac{\partial u_x}{\partial y}+\frac{\partial u_y}{\partial x}+\frac{\partial u_x}{\partial x}\cdot\frac{\partial u_x}{\partial y}+\frac{\partial u_y}{\partial x}\cdot\frac{\partial u_y}{\partial y}+\frac{\partial u_z}{\partial x}\cdot\frac{\partial u_z}{\partial y}\right)\\
\sigma_{zy} &= \sigma_{yz} = \mu\left(\frac{\partial u_y}{\partial z}+\frac{\partial u_z}{\partial y}+\frac{\partial u_x}{\partial z}\cdot\frac{\partial u_x}{\partial y}+\frac{\partial u_y}{\partial z}\cdot\frac{\partial u_y}{\partial y}+\frac{\partial u_z}{\partial z}\cdot\frac{\partial u_z}{\partial y}\right)\\
\sigma_{xz} &= \sigma_{zx} = \mu\left(\frac{\partial u_x}{\partial z}+\frac{\partial u_z}{\partial x}+\frac{\partial u_x}{\partial x}\cdot\frac{\partial u_x}{\partial z}+\frac{\partial u_y}{\partial x}\cdot\frac{\partial u_y}{\partial z}+\frac{\partial u_z}{\partial x}\cdot\frac{\partial u_z}{\partial z}\right)
\end{aligned}
\qquad \cancel{(10)}
$$

Temporal differentiation of the constitutive relation(Eq.(7)) yields velocity-stress relationships when combined with ~~Then, a first-order partial derivative with respect to~~

~~time is taken on both sides of Eq. (10), with~~ Eq. (8~~),~~).~~and the displacement~~

$$\begin{cases} \rho \dfrac{\partial v_i}{\partial t} = \dfrac{\partial \sigma_{ij}}{\partial x_j} \\ \dfrac{\partial \sigma_{ij}}{\partial t} = \lambda \delta_{ij} \dfrac{\partial E_{kk}}{\partial t} + 2\mu \dfrac{\partial E_{ij}}{\partial t} \\ \qquad = \lambda \delta_{ij} \dfrac{\partial v_k}{\partial x_k} + \mu\left(\dfrac{\partial v_i}{\partial x_j} + \dfrac{\partial v_j}{\partial x_i}\right) + \underbrace{\lambda \delta_{ij}\left(\dfrac{\partial v_k}{\partial x_m} \cdot \dfrac{\partial u_k}{\partial x_m}\right) + 2\mu \dfrac{\partial v_k}{\partial x_i} \cdot \dfrac{\partial u_k}{\partial x_j}}_{\text{additional terms}} \end{cases}, \quad i, j, k, m \in \{1,2,3\} \cancel{, i, j,}$$

~~$k \in \{x,y,z\}$~~ (~~11~~10)

~~This transforms displacement gradients into velocity terms~~where $v_i=\partial u_i/\partial t$(i∈{x, y, z})~~,~~. N~~while preserving n~~onlinear contributions emerge through velocity-displacement coupling~~:~~, whereupon ~~T~~take the~~he~~ displacement-preserving ~~nonlinear~~ terms (u_i) ~~retain~~as products of velocity components v_i ~~(i∈{x, y, z})~~ and ~~incremental displacements~~time ~~v_i~~ dt (serve as time step in simulations)~~ is converted to velocity term,~~ in the ~~velocity-stress~~ equations~~ of nonlinear elasticity used for finite-difference method are obtained in Eq. (11):~~.

$$
\begin{cases}
\dfrac{\partial\sigma_{xx}}{\partial x}+\dfrac{\partial\sigma_{xy}}{\partial y}+\dfrac{\partial\sigma_{xz}}{\partial z}=\rho\dfrac{\partial v_x}{\partial t}\\
\dfrac{\partial\sigma_{yx}}{\partial x}+\dfrac{\partial\sigma_{yy}}{\partial y}+\dfrac{\partial\sigma_{yz}}{\partial z}=\rho\dfrac{\partial v_y}{\partial t}\\
\dfrac{\partial\sigma_{zx}}{\partial x}+\dfrac{\partial\sigma_{zy}}{\partial y}+\dfrac{\partial\sigma_{zz}}{\partial z}=\rho\dfrac{\partial v_z}{\partial t}
\end{cases}
$$

$$
\begin{cases}
\dfrac{\partial\sigma_{xx}}{\partial t}=(\lambda+2\mu)\dfrac{\partial v_x}{\partial x}+\lambda\dfrac{\partial v_y}{\partial y}+\lambda\dfrac{\partial v_z}{\partial z}+dt\cdot(\lambda+2\mu)\cdot(\dfrac{\partial v_x}{\partial x}\dfrac{\partial v_x}{\partial x}+\dfrac{\partial v_y}{\partial x}\dfrac{\partial v_y}{\partial x}+\dfrac{\partial v_z}{\partial x}\dfrac{\partial v_z}{\partial x})\\
\quad +dt\cdot\lambda\cdot(\dfrac{\partial v_x}{\partial y}\dfrac{\partial v_x}{\partial y}+\dfrac{\partial v_y}{\partial y}\dfrac{\partial v_y}{\partial y}+\dfrac{\partial v_z}{\partial y}\dfrac{\partial v_z}{\partial y})+dt\cdot\lambda\cdot(\dfrac{\partial v_x}{\partial z}\dfrac{\partial v_x}{\partial z}+\dfrac{\partial v_y}{\partial z}\dfrac{\partial v_y}{\partial z}+\dfrac{\partial v_z}{\partial z}\dfrac{\partial v_z}{\partial z})\\
\dfrac{\partial\sigma_{yy}}{\partial t}=\lambda\dfrac{\partial v_x}{\partial x}+(\lambda+2\mu)\dfrac{\partial v_y}{\partial y}+\lambda\dfrac{\partial v_z}{\partial z}+dt\cdot\lambda\cdot(\dfrac{\partial v_x}{\partial x}\dfrac{\partial v_x}{\partial x}+\dfrac{\partial v_y}{\partial x}\dfrac{\partial v_y}{\partial x}+\dfrac{\partial v_z}{\partial x}\dfrac{\partial v_z}{\partial x})\\
\quad +dt\cdot(\lambda+2\mu)\cdot(\dfrac{\partial v_x}{\partial y}\dfrac{\partial v_x}{\partial y}+\dfrac{\partial v_y}{\partial y}\dfrac{\partial v_y}{\partial y}+\dfrac{\partial v_z}{\partial y}\dfrac{\partial v_z}{\partial y})+dt\cdot\lambda\cdot(\dfrac{\partial v_x}{\partial z}\dfrac{\partial v_x}{\partial z}+\dfrac{\partial v_y}{\partial z}\dfrac{\partial v_y}{\partial z}+\dfrac{\partial v_z}{\partial z}\dfrac{\partial v_z}{\partial z})\\
\dfrac{\partial\sigma_{zz}}{\partial t}=\lambda\dfrac{\partial v_x}{\partial x}+\lambda\dfrac{\partial v_y}{\partial y}+(\lambda+2\mu)\dfrac{\partial v_z}{\partial z}+dt\cdot\lambda\cdot(\dfrac{\partial v_x}{\partial x}\dfrac{\partial v_x}{\partial x}+\dfrac{\partial v_y}{\partial x}\dfrac{\partial v_y}{\partial x}+\dfrac{\partial v_z}{\partial x}\dfrac{\partial v_z}{\partial x})\\
\quad +dt\cdot\lambda\cdot(\dfrac{\partial v_x}{\partial y}\dfrac{\partial v_x}{\partial y}+\dfrac{\partial v_y}{\partial y}\dfrac{\partial v_y}{\partial y}+\dfrac{\partial v_z}{\partial y}\dfrac{\partial v_z}{\partial y})+dt\cdot(\lambda+2\mu)\cdot(\dfrac{\partial v_x}{\partial z}\dfrac{\partial v_x}{\partial z}+\dfrac{\partial v_y}{\partial z}\dfrac{\partial v_y}{\partial z}+\dfrac{\partial v_z}{\partial z}\dfrac{\partial v_z}{\partial z})\\
\dfrac{\partial\sigma_{xy}}{\partial t}=\mu(\dfrac{\partial v_y}{\partial x}+\dfrac{\partial v_x}{\partial y})+dt\cdot 2\mu\cdot(\dfrac{\partial v_x}{\partial x}\dfrac{\partial v_x}{\partial y}+\dfrac{\partial v_y}{\partial x}\dfrac{\partial v_y}{\partial y}+\dfrac{\partial v_z}{\partial x}\dfrac{\partial v_z}{\partial y})\\
\dfrac{\partial\sigma_{xz}}{\partial t}=\mu(\dfrac{\partial v_x}{\partial z}+\dfrac{\partial v_z}{\partial x})+dt\cdot 2\mu\cdot(\dfrac{\partial v_x}{\partial z}\dfrac{\partial v_x}{\partial x}+\dfrac{\partial v_y}{\partial z}\dfrac{\partial v_y}{\partial x}+\dfrac{\partial v_z}{\partial z}\dfrac{\partial v_z}{\partial x})\\
\dfrac{\partial\sigma_{yz}}{\partial t}=\mu(\dfrac{\partial v_z}{\partial y}+\dfrac{\partial v_y}{\partial z})+dt\cdot 2\mu\cdot(\dfrac{\partial v_x}{\partial y}\dfrac{\partial v_x}{\partial z}+\dfrac{\partial v_y}{\partial y}\dfrac{\partial v_y}{\partial z}+\dfrac{\partial v_z}{\partial y}\dfrac{\partial v_z}{\partial z})
\end{cases}
$$ ~~(11)~~

~~where v_i ($i\in\{x,y,z\}$) is the velocity component along the Cartesian coordinate, and dt is the time interval.~~ In addition, ~~the~~ rotation rates around ~~the~~ Cartesian ~~Coordinate~~ axes are derived from the antisymmetric rotation tensor (Eq. (4)). ~~:~~

$$
\begin{cases}
r_x=\dfrac{1}{2}(\dfrac{\partial v_z}{\partial y}-\dfrac{\partial v_y}{\partial z})\\
r_y=\dfrac{1}{2}(\dfrac{\partial v_x}{\partial z}-\dfrac{\partial v_z}{\partial x})\\
r_z=\dfrac{1}{2}(\dfrac{\partial v_y}{\partial x}-\dfrac{\partial v_x}{\partial y})
\end{cases}
$$ ~~(12)~~

Based on the ~~linear and nonlinear velocity-stress~~ ~~equations~~ ~~e~~Equ~~s. (11) and (12)~~ations, w~~W~~e implement these formulations through ~~wrote~~ C/C++ ~~language~~ code to numerically simulate ~~the propagation of~~ seismic wave~~s~~ propagation. It contains ~~To weaken boundary reflections,~~ perfectly matched ~~absorbing~~ layer (PML) ~~boundary~~ boundar~~y~~ies ~~conditions are adapted~~ to suppress ~~artificial~~ boundary reflections (Dong and Ma, 2000~~).~~), a~~A~~nd ~~–~~acoustic boundary replacement ~~method~~ (~~shown in~~ Eq. (13)) ~~is employed to ensure the application of~~for free-surface implementation~~at upper boundary, which defines the free surface condition at corresponding z-axis position~~ (Xu et al., 2007; Wang et al., 2012).

$$\begin{cases} \sigma^{0}_{zz} = 0 \\ \rho = 0.5\rho_0 \\ \lambda = 0 \\ \mu = \mu_0 \end{cases}$$ (11~~3~~)

where σ^{0}_{zz}, ρ, λ, and μ denote ~~represent the~~ normal stress, medium density, and Lamé coefficients at and above the free surface, while ~~respectively.~~ ρ_0 and μ_0 represent ~~the medium~~ density and Lamé coefficients below the free surface, respectively.

3 Simulations of basic seismic moment sources

3.1 Forward modelling parameters

~~In the physical process of seismic sources, when the seismic wavelength of interest exceeds the scale of involved source, the source can be regarded as a point source~~Seismic moment tensors provide the most complete mathematical representation of point sources when the seismic wavelength exceeds the source dimension (Gilbert, 1970~~1~~). ~~The s~~~~The symmetric second-order eismic moment tensor~~ ~~**M**, as defined represented in Eq. (14),~~As defined in Eq. (12), the symmetric second-order moment tensor **M** quantifies the equivalent force system acting at the hypocenter:~~is the most comprehensive depiction of the seismic point source (Gilbert, 1971).~~

$$M_{ij} = \mu A (v_i n_j + v_j n_i),\ i, j \in \{1, 2, 3\}\ \cancel{i, j \in \{x,y,z\}}$$ (12~~4~~)

~~w~~Where μ is the shear modulus, A the fault area, v_i the slip vector, and n_j the fault normal vector. ~~The moment tensor **M** is a symmetric second-order matrix, with each element representing a moment component acting in corresponding direction. It describes the distribution of stress at epicenter and is a crucial parameter for understanding the properties of seismic radiation fields.~~ The ~~moment~~ tensor can be decomposed into three fundamental ~~distinct~~ components: isotropy (ISO) component ~~(ISO)~~, double couple (DC) component ~~(DC)~~, and compensated linear vector dipole (CLVD) component ~~(CLVD)~~ (Knopoff and Randall, 1970; Jost and Hermann, 1989). Specifically, the ISO component represents ~~the~~ volumetric change ~~of focal area, and its moment tensor is characterized by a~~with non-zero trace and uniform force along~~in three~~ principal axes. The DC component signifies pure ~~the~~ shear dislocation without volumetric change~~dislocation of two walls of earthquake-induced fault~~ without ~~any~~ volume variation. The ~~moment tensor of the~~ CLVD component describes~~consists of~~ axial contraction/expansion with a dipole magnitude ratio 2:−1:−1~~three vector dipoles, characterized by one dipole being twice as large as the other two~~. These moment tensor expressions ~~for these three basic seismic source components~~ can be written as ~~shown below~~Eq. (13). These components govern distinct radiation patterns critical for u~~U~~nderstanding ~~the wavefield characteristics of these three representative basic seismic sources is important to understanding seismic radiation and the propagation of~~ nonlinear seismic wave propagation effects~~s~~.

$$\boldsymbol{M}^{ISO}=\begin{pmatrix} M_{11} & 0 & 0 \\ 0 & M_{22} & 0 \\ 0 & 0 & M_{33} \end{pmatrix}, \boldsymbol{M}^{DC}=\begin{pmatrix} 0 & M_{12} & 0 \\ M_{21} & 0 & 0 \\ 0 & 0 & 0 \end{pmatrix}, \boldsymbol{M}^{CLVD}=\begin{pmatrix} M_{11} & 0 & 0 \\ 0 & M_{22} & 0 \\ 0 & 0 & -2M_{33} \end{pmatrix}$$

~~(15)~~

$$\cancel{\boldsymbol{M}^{DC} = \begin{pmatrix} 0 & M_{xy} & 0 \\ M_{yx} & 0 & 0 \\ 0 & 0 & 0 \end{pmatrix}} \qquad \cancel{(16)}$$

$$\boldsymbol{M}^{CLVD} = \begin{pmatrix} M_{xx} & 0 & 0 \\ 0 & M_{yy} & 0 \\ 0 & 0 & -2M_{zz} \end{pmatrix} \qquad (13\cancel{7})$$

Following Graves(1996), ~~According to the~~we implement~~ation of seismic~~ moment tensor sources in the staggered-grid finite-difference scheme~~method Graves (1996), the~~ by converting body force ~~represented by the moment tensor can be converted into a velocity source by adding it~~ to equivalent velocity sources~~components~~. The ~~specific~~ loading equations for the three moment sources~~ in the grid system~~ are shown in Eq~~s~~. (14~~8~~)~~, (19), and (20)~~.

$$\begin{aligned}
\boldsymbol{M}^{ISO} &: \Delta v_i^n = \frac{M_{ij} \cdot dt \cdot f^n}{\rho V} \cdot \frac{\partial}{\partial x_j} \\
\boldsymbol{M}^{DC} &: \Delta v_i^n = \frac{M_{jk} \cdot dt \cdot f^n}{\rho V} \cdot \left(\delta_{ij} \frac{\partial}{\partial x_k} + \delta_{ik} \frac{\partial}{\partial x_j}\right) \\
\boldsymbol{M}^{CLVD} &: \Delta v_i^n = \frac{M_{kl} \cdot dt \cdot f^n}{\rho V} \cdot \left(\delta_{ik} \frac{\partial}{\partial x_l} + \delta_{il} \frac{\partial}{\partial x_k} - \frac{2}{3} \delta_{kl} \frac{\partial}{\partial x_i}\right)
\end{aligned} \qquad (14\cancel{8})$$

$$\cancel{\mathrm{DC}: \Delta v_i^n = \frac{M_{jk} \cdot dt \cdot f^n}{\rho V} \cdot \left(\delta_{ij} \frac{\partial}{\partial x_k} + \delta_{ik} \frac{\partial}{\partial x_j}\right)} \qquad \cancel{(19)}$$

$$\cancel{\mathrm{CLVD}: \Delta v_i^n = \frac{M_{kl} \cdot dt \cdot f^n}{\rho V} \cdot \left(\delta_{ik} \frac{\partial}{\partial x_l} + \delta_{il} \frac{\partial}{\partial x_k} - \frac{2}{3} \delta_{kl} \frac{\partial}{\partial x_i}\right)}$$

$$\cancel{(20)}$$

where $i, j, k, l \in \{1,2,3\}$. Δv denotes ~~is the~~ velocity increment, n the ~~and *dt* are the~~ time step index, ~~node and~~dt the time interval, ~~and~~ ρ material density, and V grid cell~~are the medium density and the unit~~ volume~~ of the model~~. The source-time function f^n using~~es~~ a Ricker wavelet~~corresponds to~~ with ~~the amplitude of wavelet~~wavelet amplitude at $n\,dt$~~moment~~.

To exclude effects on nonlinear wave propagation from complex medium characteristics, ~~In the~~For ~~numerical~~ implementation~~simulations, the Ricker wavelet with a~~ 0.5 Hz ~~dominant frequency of 0.5 Hz was utilized as the source wavelet.~~ we currently ~~In order to~~ focus exclusively~~on the influence of nonlinearity~~ on ~~seismic waves generated by different types of moment sources, we currently only discuss the~~ simulations in a 3D homogeneous isotropic full-space model. The numerical implementation employs the Ricker wavelet with a 0.5 Hz dominant frequency. The model spans~~size is~~ 80 km (x) × 80 km (y) × 80 km (z)~~,~~ with a uniform grid spacing of ~~0.5 k~~500 meters ~~grid division~~ in ~~the three~~X, Y, and Z directions. Material~~The medium physical~~ properties are: P-wave velocity v_p=4400 m/s, S-wave velocity v_s=3000 m/s, and density ρ=2600 kg/m^3. The ~~epicenter~~ source resides~~is located~~ at the model center ~~of the model~~ (40 km, 40 km, 40 km). T~~he time sampling interval~~emporal discretization uses Δt = ~~is~~ 15 ms~~, and the total recording time spans~~ over ~~9 seconds~~s ~~duration~~, ~~using~~ with second-order differential accuracy in time and sixth-order ~~spatial difference~~in space ~~differences~~ ~~approximation~~.

For Numerical stability, based on the simulation parameters, the spatial discretization achieves ~~12~~10.4 ($v_s/\Delta/f_{dominant}$) points per wavelength for the dominant frequency, ~~calculated as: PPW =~~ ~~$v_p/\Delta x \cdot f_{dominant}$~~ ~~= 4400m/s/500m·0.5Hz = 17.6 PPW (upper bound at Nyquist frequency: 12 PPW). This PPW criterion~~which exceeds the 8–10 PPW threshold for sixth-order schemes to suppress numerical dispersion artifacts (Virieux, 1986). Follows t~~T~~he temporal stability ~~follows the~~of 3D Courant-Friedrichs-Lewy (CFL) criterion ($\Delta t \cdot v_{max} \cdot \mathrm{sqrt}(1/\Delta x^2+1/\Delta y^2+1/\Delta z^2)$), ~~: CFL =~~ ~~$\Delta t \cdot v_{max} \cdot \mathrm{sqrt}(1/\Delta x^2+1/\Delta y^2+1/\Delta z^2)$ = 0.01s·4400m/s·sqrt(3×(500 m)$^{-2}$)~~ ≈it reaches about

0.16~~/~~. The resultant CFL number ~~represents~~is a conservative value relative to the empirical 3D stability limit of 0.5 (Moczo et al., 2007), ensuring waveform fidelity while accommodating potential nonlinear term amplification~~. ensuring robust second-order time integration while maintaining waveform fidelity~~.

3.2 Simulation r~~R~~esults

3.2.1 ISO source

~~Under the wave equations containing nonlinearity in small deformation,~~ Fig. 3a displays ~~8th second~~ 6C wavefield snapshots at 8 seconds ~~induced~~ for~~by~~ the ISO source under nonlinear deformation condition.~~,~~ Translational components exhibit ~~revealing~~ uniform ~~consistent~~ P-wave amplitudes, while ~~in translational components but near absence in~~ rotational components show near- absence of P-wave energy. T–

~~Fig. 3b highlights t~~the wavefield differences between linear and nonlinear simulations (Fig.3b) ~~between linear and nonlinear conditions,~~ reveal ~~showing that P waves persist in translational components~~ emergent S-wave signatures~~but are very weak in rotation, where S waves unexpectedly emerge~~. ~~This,~~ contrastings with classical elastodynamic theory,~~,~~ where ISO sources ~~generate exclusively~~exclusively generate P-waves~~, and~~ in homogeneous isotropic media~~linear theory,~~ ~~since the~~through pure ~~volume change of elastic material is solely associated with a pure pressure field of~~ compressional/~~ or~~ expansional volume change. ~~So, only~~The anomalous ~~P-waves propagate in homogeneous and isotropic media. However, Fig. 3b demonstrates unique nonlinear media characteristics, enabling~~ P-S ~~wave~~ coupling phenomenon arises from nonlinear volumetric-shear strain interactions governed by the constitutive relationship (Eq. (7))~~and energy conversion. This occurs due to nonlinear volumetric strain terms related to shear strains, disrupting linear theory's independent P-S wave propagation constraint~~, where the higher-order terms ~~facilitate~~enable energy transfer between compressional and shear deformation modes.

Fig. 4 quantified the relative change between linear and nonlinear simulations at each grid cell volume. We applied a stability threshold to the relative change calculations to mitigate the influence of unrealistic wavefields ($value_{linear} \rightarrow 0$). It can be seen from Fig.4 that (i) the spatial distribution exhibits general symmetry and homogeneity with alternating positive/negative anomalies (Fig. 4a), where negative values (<0) indicate overestimation by linear theory ~~while~~and positive values (>0) suggest underestimation; (ii) rotational components ~~show~~have different and more complex azimuthal distribution and larger~~higher magnitudes of~~ relative changes than translational components~~ (Fig. 4b)~~, also evidenced by ~~broader~~ probability density function (PDF) distributions in (Fig. 4b).

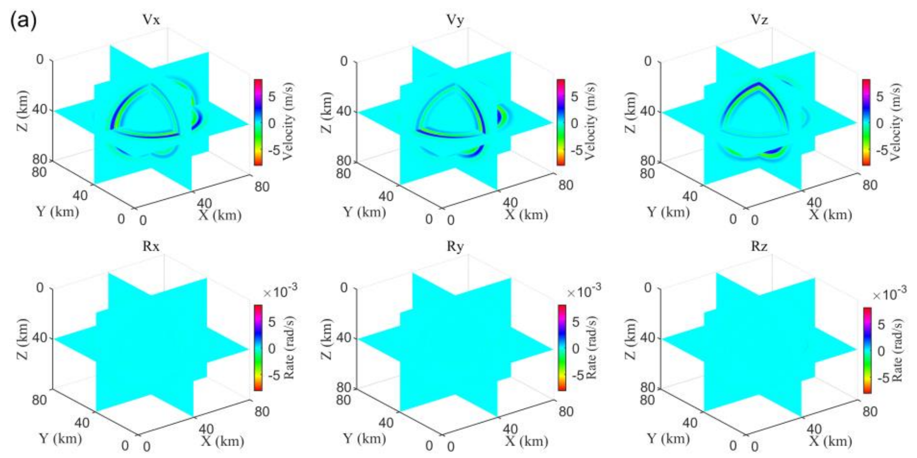

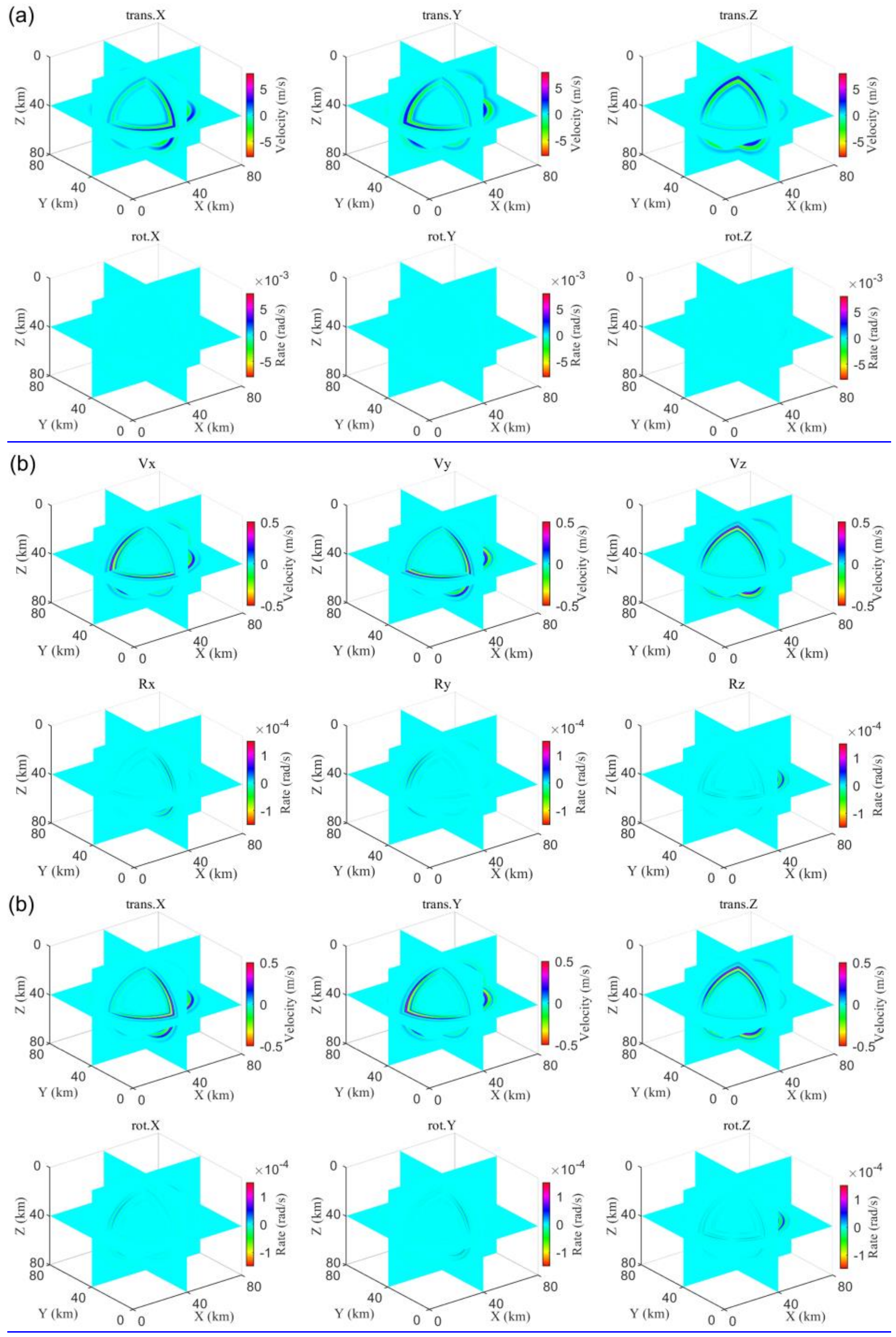

Figure 3. ~~Snapshots of~~ (a) Nonlinear 6C wavefield ~~in nonlinear model~~ and (b) linear-nonlinear discrepancy for~~wavefield difference between linear and nonlinear models~~ Mw7 ISO source at ~~8th second excited by ISO source (Mw7)~~t=8s.

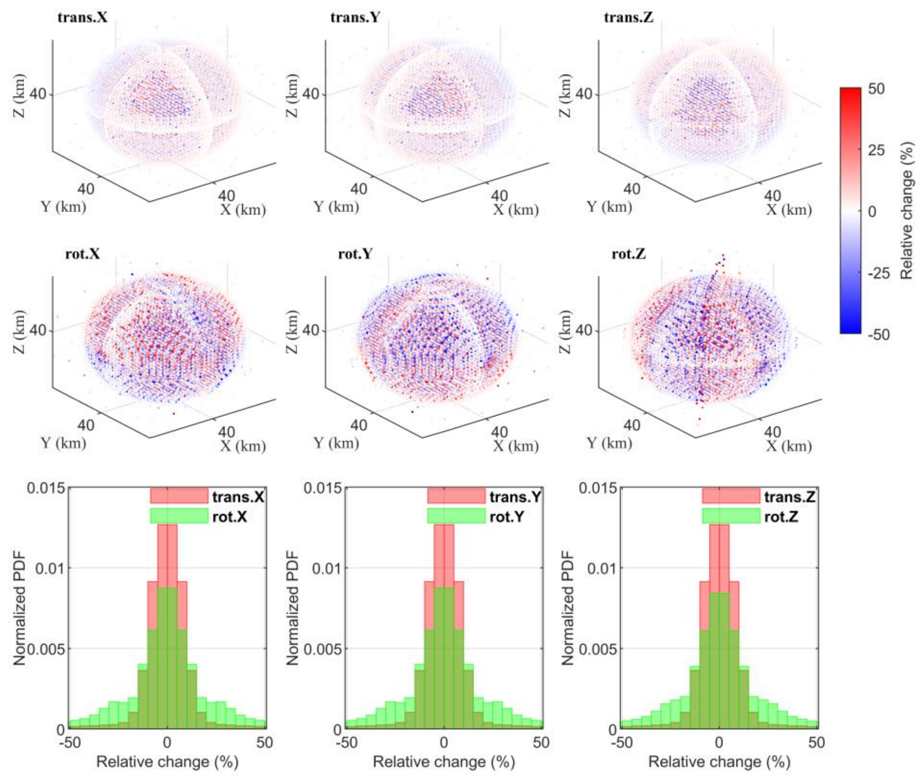

Figure 4. ISO source linear-nonlinear relative change: (a) 3D spatial distribution (b) Probability density function.

3.2.2 DC source

Fig. 5a presents 6C ~~The~~ wavefield~~s~~ snapshots for~~excited by~~ the DC source ~~in the~~ under nonlinear conditions.~~model are illustrated in Fig. 4a. The DC source primarily generates S waves with higher energy, with P-waves being comparatively weaker. The loaded force couple, Mxy and Myx, enhances the waves in the Vx and Vy components relative to the Vz component. Similarly, the Rz component waves are more pronounced than in the Rx and Ry components.~~ The w~~W~~avefield difference between nonlinear and linear wavefields ~~difference~~ in Fig. 5~~4~~b demonstrates a different wavefront ~~shows nearly one order of magnitude difference in intensity between the difference wavefields and the original wavefields. P- and S-wave~~

~~intensities are nearly equal in translational components, while S waves dominate in Rx and Ry components.~~

~~In addition, Fig. 4b reveals distinct wavefront polarities for P and S waves influenced by nonlinear terms, differing from those in Fig. 4a. This indicates that nonlinear effects on seismic waves from DC-type source may differ from those of ISO-type source. That is, nonlinearity's impact on seismic waves from shear force sources contrasts with pressure sources, potentially being more complex and leading to the deviations of polarity of wavefield from the original wavefield.~~energy distribution from the original wavefront distribution in Fig. 5a. This energy redistribution caused by nonlinearity~~,~~ indicat~~ing~~es that shear-dominated sources induce more complex nonlinear interactions.

The relative changes of nonlinear effects ~~From~~ (Fig. 6)~~, nonlinear effects show~~ reveal not only ~~distinct angular~~ zone variation but also localized strong nonlinearities at axial positions related to the distribution of the force couples tied to the DC source of fault displacement directions~~.~~. At the same time, rotational components show a similar spatial distribution of underestimated and overestimated areas and localized strong nonlinearities, and rot.X and rot.Y components show larger change values, as seen from the PDF results.

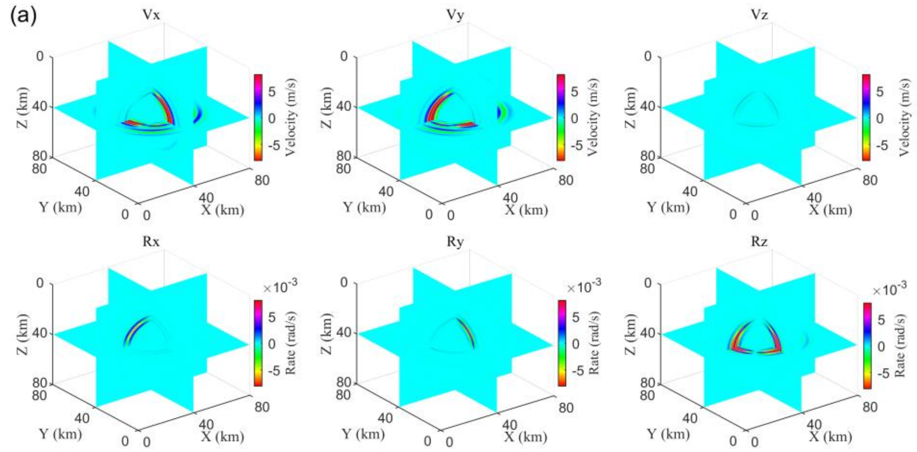
(a)
Vx
Vy
Vz
Rx
Ry
Rz
Velocity (m/s)
Rate (rad/s)
Z (km)
Y (km)
X (km)

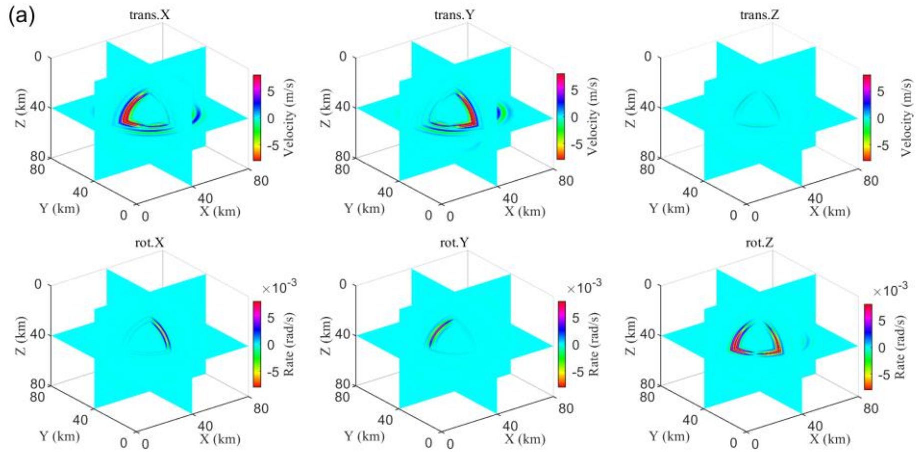
(a)
trans.X
trans.Y
trans.Z
rot.X
rot.Y
rot.Z
Velocity (m/s)
Rate (rad/s)
Z (km)
Y (km)
X (km)

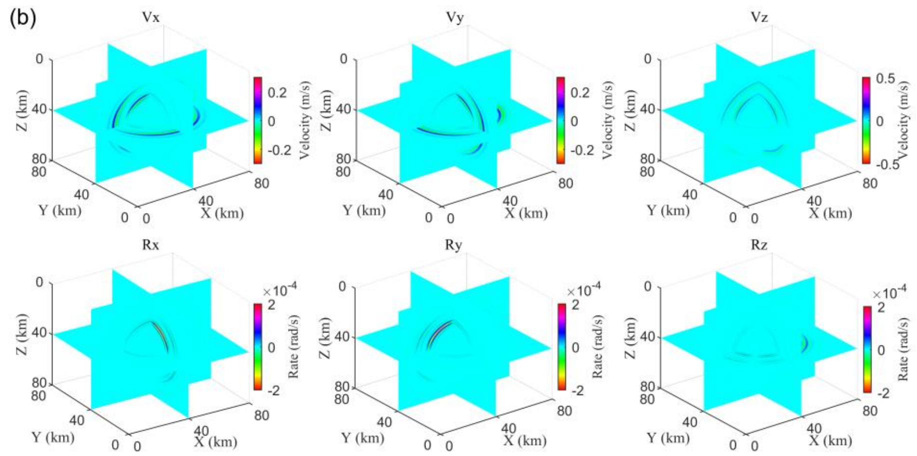
(b)
Vx
Vy
Vz
Rx
Ry
Rz
Velocity (m/s)
Rate (rad/s)
Z (km)
Y (km)
X (km)

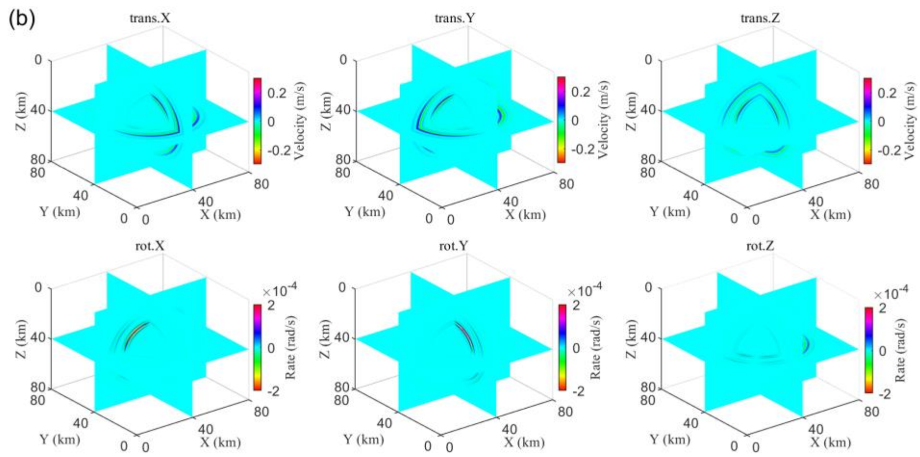
(b)
trans.X
trans.Y
trans.Z
rot.X
rot.Y
rot.Z
Velocity (m/s)
Rate (rad/s)
Z (km)
Y (km)
X (km)

Figure ~~4~~5. (a) Nonlinear 6C wavefield and (b) linear-nonlinear discrepancy for Mw7 DC source at t=8s.~~Snapshots of (a) 6C wavefield in nonlinear model and (b) wavefield difference between linear and nonlinear models at 8th second excited by DC source (Mw7)~~

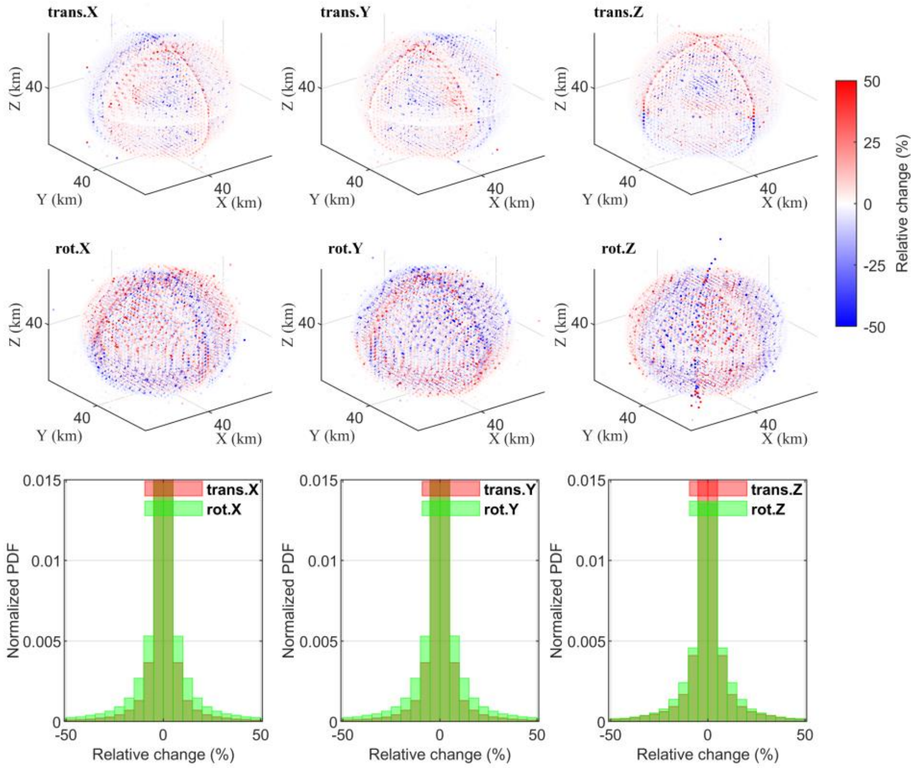

Figure 6. DC source linear-nonlinear relative change: (a) 3D spatial distribution (b) Probability density function.

3.2.3 CLVD source

Figs. 7~~5a~~ displays the results ~~-~~for the CLVD source simulation, ~~showing~~ demonstrating ~~(i). The intensities of P- and S-waves are approximately equal in the translational components, whereas S~~S-waves dominance in ~~in the~~ rotational components~~, S-waves dominate with the Rz component being notably weaker. (ii)~~ and

~~The consistent~~its linear-nonlinear discrepancy~~discrepancies shown~~ in Fig. 7~~5~~b highly resembles~~with that observed in~~ DC source results ~~simulations~~ (Fig. 5b)~~.~~, ~~emphasize the significant intensity of S-wave discrepancies in the rotational components, underscoring their superiority in capturing S-waves propagating through nonlinear media.~~

~~It is evident that the polarity of wavefield discrepancies due to nonlinearity in the CLVD source simulation aligns with that observed in the DC source simulation (Fig. 4b). The results may suggest that since both CLVD and DC-type force sources generate seismic waves in a non-volumetric manner, nonlinearity leads to particularly prominent volume changes due to shear stresses.~~ reflecting their~~These~~is shared wavefield differences caused by nonlinearity for CLVD and DC source simulations may emerge from their fundamental kinematic similarity as non-volumetric source mechanisms.

Fig. 8 demonstrates~~ (i) z~~ Z-axis aligned ~~dipole-constrained~~ anomalies corresponding to ~~distribution aligned with~~ the CLVD compression axis~~ (z-axis)~~ for translational and rotational components~~; (ii)~~, while the PDF distributions show overall enhanced nonlinear responses in rotational components~~ overall stronger nonlinear responeses~~. The observed patterns correlate with the used CLVD source mechanism's kinematic characteristics — axial compression of twice the force along Z and extension in x/y directions — demonstrating how nonlinear effects inherit source radiation features while introducing directional dependence.

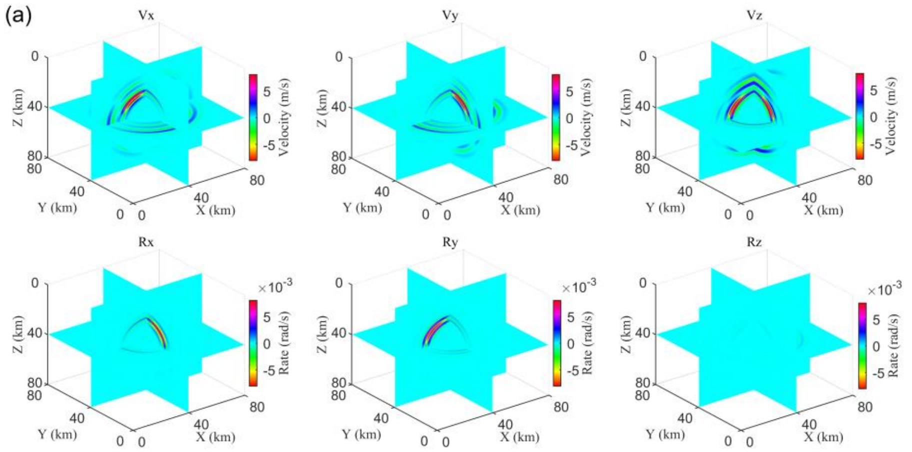
(a)
Vx
Vy
Vz
Velocity (m/s)
Rx
Ry
Rz
Rate (rad/s)
Z (km)
Y (km)
X (km)

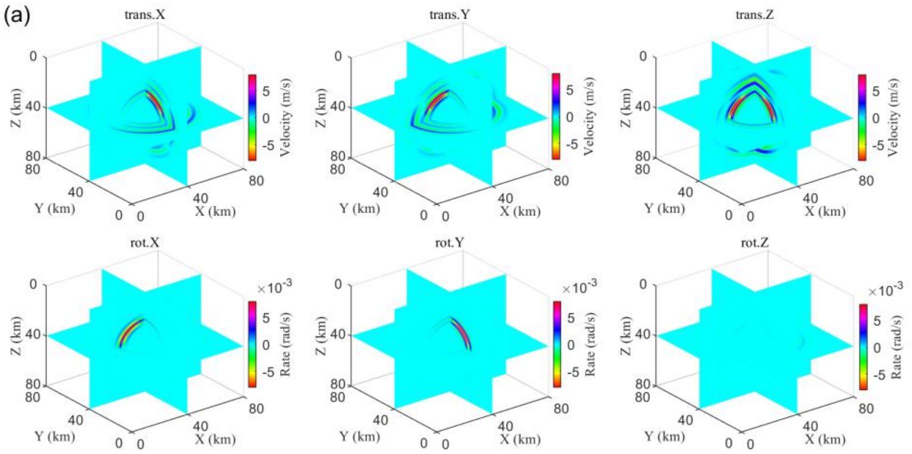
(a)
trans.X
trans.Y
trans.Z
Velocity (m/s)
rot.X
rot.Y
rot.Z
Rate (rad/s)
Z (km)
Y (km)
X (km)

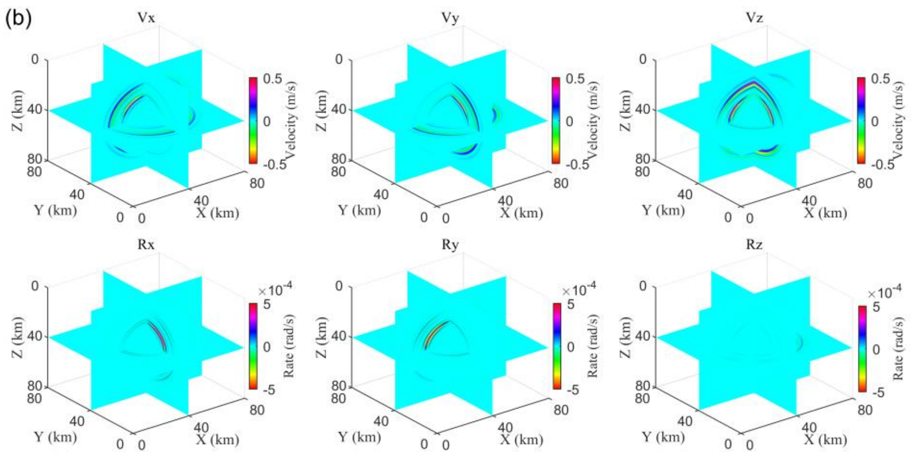
(b)
Vx
Vy
Vz
Velocity (m/s)
Rx
Ry
Rz
Rate (rad/s)
Z (km)
Y (km)
X (km)

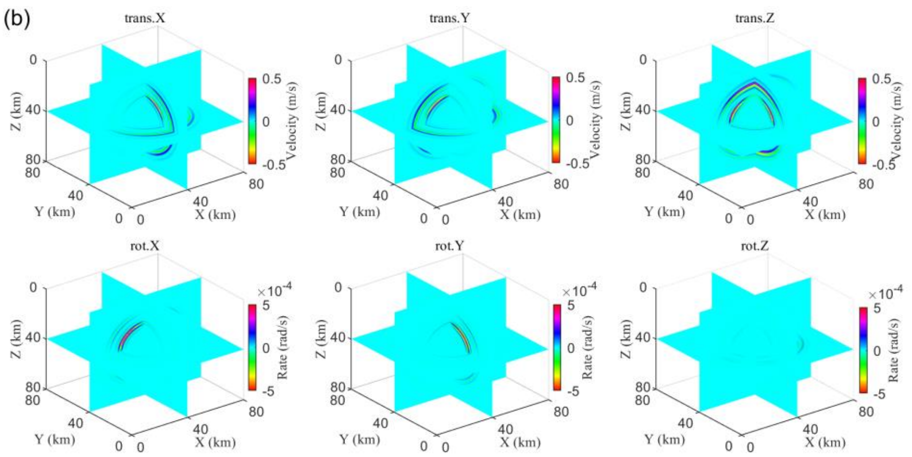
(b)
trans.X
trans.Y
trans.Z
Velocity (m/s)
rot.X
rot.Y
rot.Z
Rate (rad/s)
Z (km)
Y (km)
X (km)

Figure 7~~5~~. (a) Nonlinear 6C wavefield and (b) linear-nonlinear discrepancy for Mw7 CLVD source at t=8s.~~Snapshots of (a) 6C wavefield in nonlinear model and (b) wavefield difference between linear and nonlinear models at 8th second excited by CLVD source (Mw7)~~

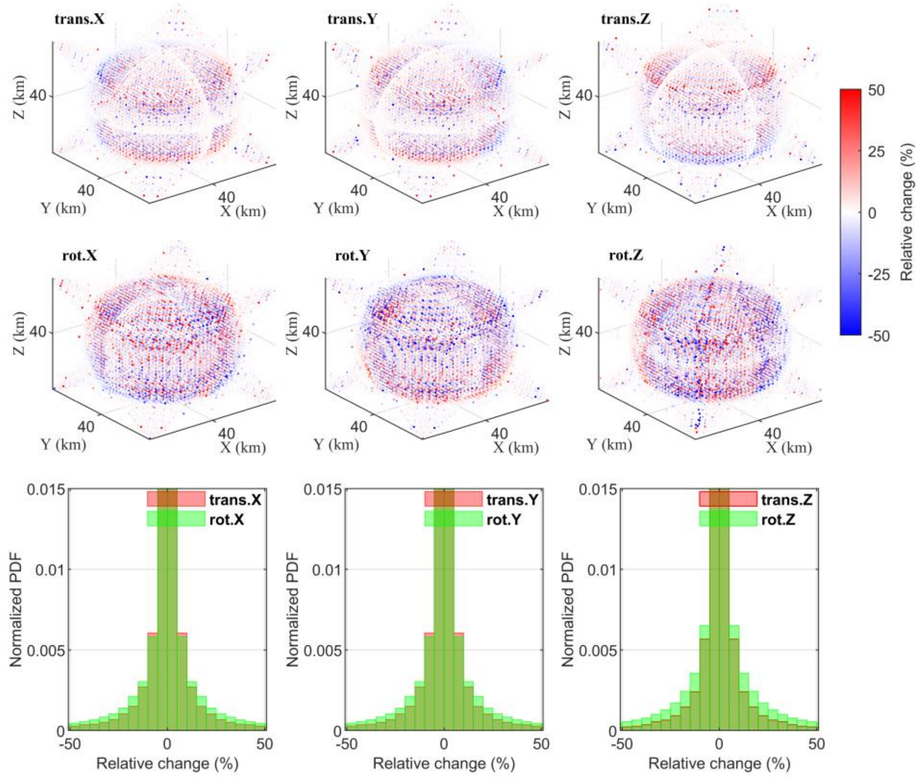

Figure 8. CLVD source linear-nonlinear relative change: (a) 3D spatial distribution (b) Probability density function.

The three force source types exhibit distinct nonlinear signatures governed by their fundamental characteristics. ISO sources generate more homogeneous spatial nonlinear effects. CLVD sources amplify directional nonlinear anomalies along principal strain axes. DC sources primarily restrict local stronger nonlinear effects to the force-couple axis. These differences emerge from how each source type interacts with the nonlinear strain tensor in Eq. (2). The cross-term 1/2 r$u_k/\partial u_i \cdot \partial u_k/\partial u_j$ enables energy transfer between deformation modes and violates the linear theory's strict P-S decoupling. Rotational components demonstrate particular sensitivity to these higher-order interactions, as evidenced by their broader PDF distributions across all source types. This source-dependent nonlinear behavior underscores the importance of considering rotational wavefield components and source kinematics when interpreting strong ground motions.

3.3 Wavefield comparisons

~~Figure 9 quantifies~~The nonlinear effects on seismic wavefields are qualified through relative energy change (ΔE) throughout the entire simulat~~ed~~ion domain ~~space by~~ using Eq. (~~21~~15) and the sensitivity ratio of rotational to translational ($\Delta E_{rot}/\Delta E_{trans}$).~~The comparison highlights disparities in wavefields of nonlinear elastic waves across both translational and rotational components. We synthesized the seismic wavefield for moment magnitudes ranging from 2 to 7 and analyzed wavefield energy E variations at 6th second of propagation for the three source simulations in both nonlinear and linear models (Fig. 6). The wavefield energy was approximated using Eq. (21):~~

$$\Delta E = \frac{E_{nonlinear} - E_{linnear}}{E_{linnear}} \times 100\%, \quad E = \sum_{i,j,k} v_{i,j,k}^{2} \Delta V \qquad (\cancel{21}15)$$

where $v_{i,j.k}$ is ~~the~~ wavefield value at each grid point~~,~~ and ΔV is ~~the~~ unit grid cell volume.

~~Fig. 6 displays variations in nonlinear effects across moment magnitudes. The ISO source (Fig. 6a) exhibits a more significant relative error in the wavefield compared to the CLVD source (Fig. 6b), while the DC source (Fig. 6c) yields the most minor~~

~~relative error among the three models. Across these sources, the wavefield energy change rate increases exponentially with magnitude. At magnitude 7, the rate reaches 10% for the ISO source and 5% for the CLVD source. For magnitudes below 4, nonlinear effects are minimal. However, in moderate-to-large earthquakes (magnitudes > 4), the relative alteration in the rotational components becomes more substantial than in the translational components. Given that the DC source typically dominates focal mechanisms for most earthquakes (Zhao and Zhang, 2022), we infer that the linear approximation suffices for modeling most earthquakes (solely involving body waves). However, this approximation may break down in intense seismic activity, particularly when considering rotational components.~~~~As illustrated in Fig. 9 and Table 2,~~Fig. 9 illustrates –the ~~nonlinear effects on~~ global energy variations between nonlinear and linear simulations at 6th seconds for ISO, CLVD, and DC sources~~exhibit distinct patterns across source mechanisms~~. As the magnitude increases, the relative change of global wavefield energy shows an exponential increase, with sufficiently larger values of relative change when it reaches Mw 5. The ISO source exhibits the most pronounced nonlinear effects, with relative energy changes reaching 10.03% (translational) and 22.87% (rotational) at Mw7 (Fig. 9a, Table 1). This contrasts with CLVD and DC sources showing smaller changes (CLVD: 3.64% translational, 6.41% rotational; DC: <1% in all components). ~~As the magnitude increases, the relative change of global wavefield energy shows an exponential increase, with larger values of relative change when it reach than Mw 4.~~

The ISO source introduces uniform energy amplification in seismic components through nonlinear dilatational enhancing strain accumulation. The CLVD and DC sources redistribute localized energy, suppressing net energy changes, especially for the DC source.

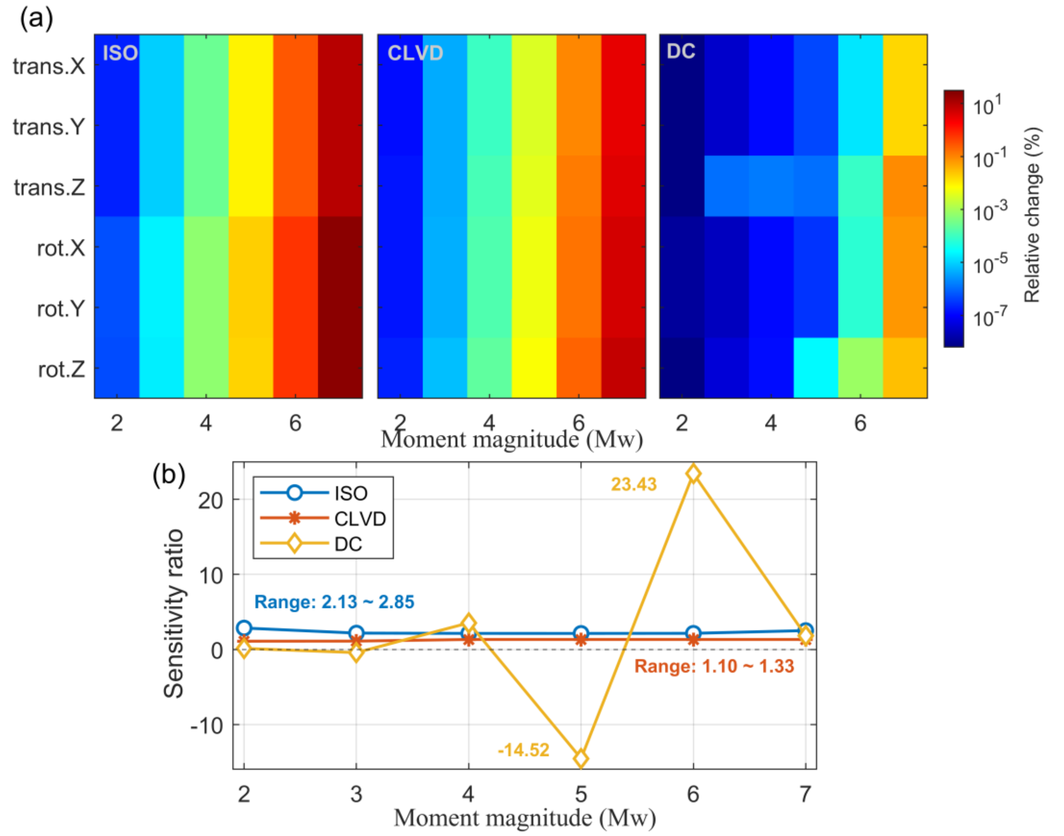

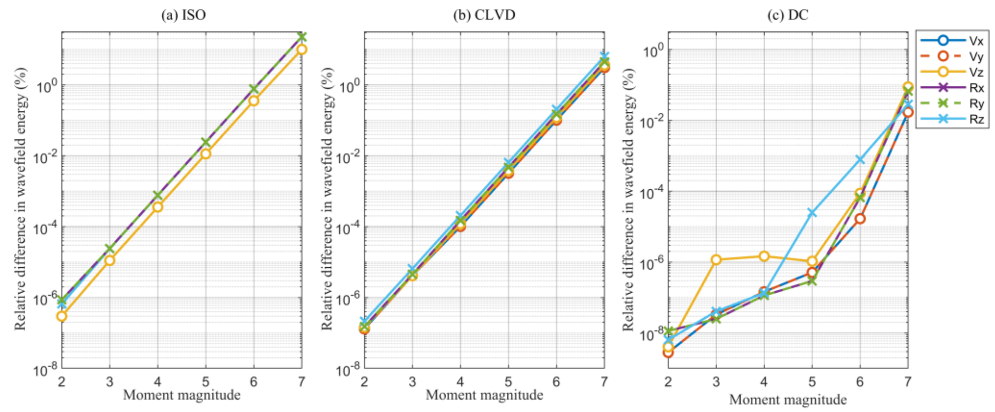

Figure ~~6~~9. Relative energy changes ~~in wavefield energy~~ induced by nonlinearity ~~in the simulations~~ of (a) ~~ISO, (b) CLVD, and (c) DC~~the three seismic sources at 6th second with increasing moment magnitude and sensitivity ratio of rotation vs.

translation.

Table ~~2~~1. Global wavefield energy change characteristics.

Source type	Max ΔE_{trans} (%, Mw7)	Max ΔE_{rot} (%, Mw7)	Sensitivity (rot./trans.)
ISO	10.03 (trans.)	22.87 (rot.)	2.13 ~ 2.85
CLVD	3.64 (trans.Z)	6.41 (rot.Z)	1.10 ~ 1.33
DC	0.03 (trans.Z)	0.09 (rot.Z)	extremes: -14.52, 23.43

~~Fig. 7 showcases the temporal evolution of wavefield energy between nonlinear and linear models for a magnitude 6 earthquake. Within the first 4 to 6 seconds of seismic wave propagation, intricate phase interactions may result in an overall energy reduction. Subsequently, wavefield energy difference due to nonlinearity stabilizes, with a more significant energy increase in the rotational component than the translational components. The ISO source model exhibits the most prominent increase in nonlinear relative error with wave propagation, followed by CLVD-type source (Fig. 7b). In the DC source model, nonlinear effects are minimal, with negligible changes induced by nonlinearity in all components except the Rz component (Fig. 7c).~~

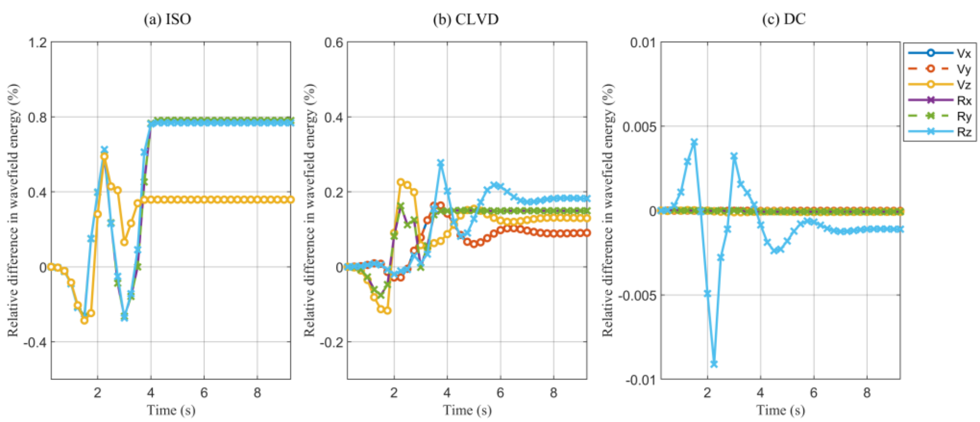

~~**Figure 7.** Relative changes in wavefield energy induced by nonlinearity in the simulations of (a) ISO, (b) CLVD, and (c) DC sources (Mw6) with increasing time~~

~~Based on the preceding results, current seismometers possess sufficient accuracy to capture nonlinearity-induced anomalies in wavefield intensity as demonstrated in simulations. However, it is crucial to observe that these simulations exhibiting prominent anomalies utilize larger magnitude seismic sources and model wave propagation over approximately 30 km, representing near-field results. Under such circumstances, the manifestation of nonlinear effects is anticipated to be significant.~~

~~In contrast, capturing the nonlinearity on seismic waves in small magnitudes or distant seismicity poses greater challenges. The attenuation and scattering of seismic waves with distance and the relatively lower energy released by smaller magnitudes. Consequently, nonlinear effects may be substantially weakened, heightening the complexity of observation and identification. Thus, given current technological and observational constraints, studying the nonlinear effects of strong earthquakes emerges as a more practical and feasible option.~~

The simulation results demonstrate that rotational measurements enhance nonlinear detection capability by 1-3× compared to traditional translational components. ~~modern~~Current broadband seismometers possess sufficient resolution~~the resolution necessary~~ to detect these nonlinear wavefield anomalies. However, two critical constraints govern actual observational feasibility~~, including~~: magnitude-distance threshold and small/distant event challenges.

Pronounced nonlinear signatures manifest primarily in large-magnitude events (Mw ≥5) within near-field distances (simulated 30 km). This arises from strain amplitudes exceeding 10^{-4}—the empirical threshold for detectable nonlinear coupling (Guyer and Johnson, 1999), and limited geometric spreading and attenuation in proximal regions. For smaller magnitudes (Mw <5) or far-field observations, nonlinear strain amplitudes decay below, obscured by ambient noise floors, and path effects (scattering, attenuation) and source radiation patterns disperse nonlinear signatures. Given current instrumental limits (e.g., rotational sensor of a self-noise up to 2×10^{-8} $rad/s/\sqrt{Hz}$), targeted studies of near-field and moderate to strong earthquakes offer the most viable pathway to characterize nonlinear constitutive laws.

4 Earthquakes ~~Observations and~~ simulations ~~of two earthquakes~~

Building upon the theoretical framework for fundamental source types, we extend our simulations to more complex scenarios incorporating realistic source mechanisms and layered media. Analyzing two moderate-magnitude earthquakes (E1: Mw5.4 and E2: Mw6.1) along the Taiwan coast aims to validate theoretical predictions of nonlinear wave propagation and establish baseline understanding for future observational comparisons. The events were respectively recorded at stations NA01 (E1) and QS01 (E2) (Chen et al., 2023), as shown in Fig. 10, depicted by GMT (Wessel et al., 2019). Moment tensor solutions derived from the U.S. Geological Survey (USGS) are defined in Eq. (16), with synthetic 6C seismograms generated under both linear and nonlinear constitutive relations. ~~To investigate nonlinear seismic~~

wave propagation, we Two earthquakes along the Taiwan coast are referenced to establish seismic models for simulating wave propagation in both linear and nonlinear media based on two earthquakes (E1 and E2) along the Taiwan coast (Chen et al., 2023). ,. The moment tensor solutions parameters of for E1 and E2, derived from the U.S. Geological Survey (USGS, https://www.usgs.gov/) are explicitly defined detailed in Eqs. (22) and (23), respectively.

4.1 Hualien earthquakes

Taiwan, situated at the juncture of three prominent tectonic plates—the Philippine Sea Plate, the Eurasia Plate, and the Pacific Ocean Plate—experiences frequent moderate to large earthquakes annually (Zheng et al., 2005). The 2018 Hualien earthquake (M_W 5.41, referred to as E1) and the 2019 Hualien earthquake(M_W 6.13, referred to as E2) occurred along Taiwan's eastern coastline, with 15 km and 30 km epicenter depths, respectively. The epicenter locations and station configurations, as depicted by GMT (Wessel et al., 2019), are shown in Fig. 8. To directly observe seismic rotational rates, BlueSeis-3A fiber-optic rotational seismometers, characterized by a self-noise of up to 2×10^{-8} $rad/s/\sqrt{Hz}$ and a bandwidth of 0.001-100 Hz (Bernauer et al., 2018; Cao et al., 2021) were deployed at the Nanao station (NA01) to record E1 and at the Qingyuanshan station (QS01) to record E2.

According to the information from the U.S. Geological Survey (USGS, https://www.usgs.gov/), both E1 and E2 were triggered by reverse faulting mechanisms. The focal mechanisms represented by beach balls are shown in Fig. 8b. The moment tensor parameters of E1 and E2 are detailed in Eqs. (22) and (23),

~~respectively.~~

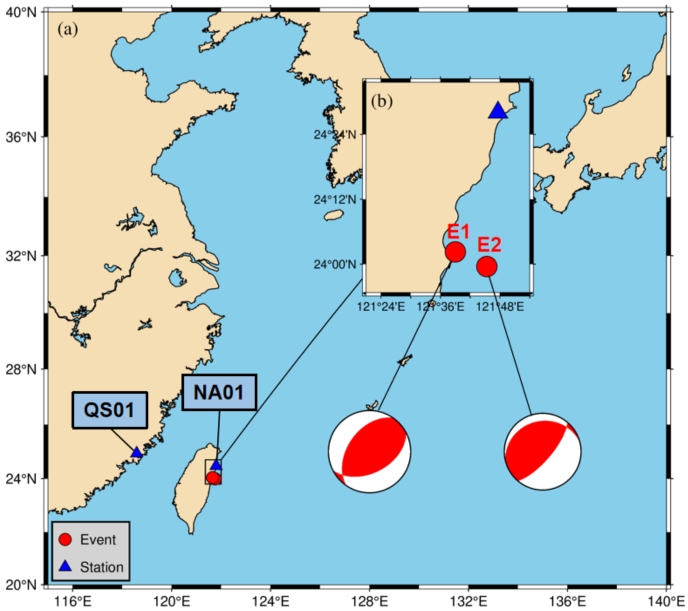

Figure 10~~8~~. Epicenters and observation sites of E1 and E2

$$E1:\begin{bmatrix} M_{xx}=-7.569\times10^{16}, M_{yy}=-2.373\times10^{16}, M_{zz}=9.942\times10^{16} \\ M_{xz}=7.372\times10^{16}, M_{yz}=-1.0965\times10^{17}, M_{xy}=4.156\times10^{16} \end{bmatrix}$$
$$E2:\begin{bmatrix} M_{xx}=-1.064\times10^{18}, M_{yy}=-7.607\times10^{17}, M_{zz}=1.8247\times10^{18} \\ M_{xz}=3.141\times10^{17}, M_{yz}=3.155\times10^{17}, M_{xy}=1.114\times10^{18} \end{bmatrix}$$
(16~~22~~)

To isolate source-related nonlinearity, we simulate both earthquakes adopting the a simplified laterally homogeneous crustal model based on CRUST1.0 (Laske et al., 2013), with physical properties and simulation parameters listed in Tables 2 and 3. Free-surface condition is used at the top, and perfectly matched layer (PML) condition is used on other boundaries, with 10-order differential accuracy in space.

$$\frac{M_{xx}=-1.064\times10^{18}, M_{yy}=-7.607\times10^{17}, M_{zz}=1.8247\times10^{18}}{M_{xz}=3.141\times10^{17}, M_{yz}=3.155\times10^{17}, M_{xy}=1.114\times10^{18}}$$
~~(23)~~

~~These simulations aim to preliminarily assess the nonlinear effects of more complex seismic source mechanisms. The spatial difference accuracy in these~~

~~simulations is set to 10~~

~~4.2 Earthquake simulations~~

Table ~~1~~ 32. Physical properties of ~~media for simulations of E1 and E2~~layered media.

Layer	Thickness (km)	vp (km/s)	vs (km/s)	ρ (kg/m^3)
1	0.50	2.50	1.07	2.11
2	10.12	5.80	3.40	2.63
3	9.81	6.30	3.62	2.74
4	9.82	6.90	3.94	2.92
5	-	7.70	4.29	3.17

~~**Table 2** Simulation parameters for E1~~

~~Items~~	~~Parameters~~
~~Source type~~	~~Eq. (20)~~
~~Central frequency~~	~~1 Hz~~
~~Grid interval~~	~~1 km~~
~~Time interval~~	~~5 ms~~
~~Source location~~	~~(0, 0, 15 km)~~
~~Receiver location~~	~~(53 km, 4 km, 0 km)~~
~~Recording time~~	~~30 s~~

Table 43 Simulation parameters ~~for E1~~

Iterm	Paremeter (E1, E2)
Dominant frequency	1 Hz, 0.5 Hz
Moment magnitude	Mw5.4, Mw6.1
Depth	15 km, 30 km
Grid spacing	1 km, 2 km
Time step	5 ms, 2 ms
Source mechanisms	Eqs. (16)
Spatial differential accuracy	10th order

~~Fig. 10 presents a comparision of 6C root-mean-square (RMS) amplitude (Fig. 10a) and normalized time-frequency spectrum difference (Fig. 10b) between linear and nonlinear seismic models. RMS amplitudes within a 2-second window were computed at 1-second intervals, with relative change rates derived.~~

~~Fig. 10a reveals minor RMS amplitude anomalies attributed to nonlinearity, with the rotational components smaller than the translational components, and translational errors not exceeding 0.1%. For the E1 simulation, linear approximation errors are negligible. In Fig. 10b, the seismic phases affected vary in translational and rotational components. Rotational components exhibit greater impact of nonlinearity on direct S-waves and surface waves, whereas in the translational components, particularly in Vx and Vz, nonlinearity shows heightened effects on p-waves, with the surface waves in the Vy component also affected.~~

Fig~~ure~~. 11a presents the simulated 6C seismic records for E1 in radial (R), transverse (T), and vertical (Z) coordinates, demonstrating prominent amplitude predominance in the trans.Z and rot.T components. Nonlinear effects manifest as subtle RMS amplitude changes (<1%), with rotational anomalies weaker than translational counterparts (Fig. 11b). Normalized time-frequency spectral differences further highlight distinct nonlinear patterns across components and wave phases~~.~~: direct –and reflected waves show larger RMS amplitude changes in trans.R and Z components, while surface waves in trans.T component display the strongest nonlinear sensitivity. S-waves in rot.R and T components and surface waves in rot.Z component show enhanced nonlinear effects, and Love-wave nonlinear perturbations in rot.Z component remain relatively weak.~~Rotational components exhibit stronger nonlinear effects in S-waves and surface waves,.~~

~~Rotational components exhibit greater impact of nonlinearity on direct S-waves and surface waves, whereas in the translational components, particularly in Vx and Vz,~~

~~nonlinearity shows heightened effects on p-waves, with the surface waves in the Vy component also affected.~~

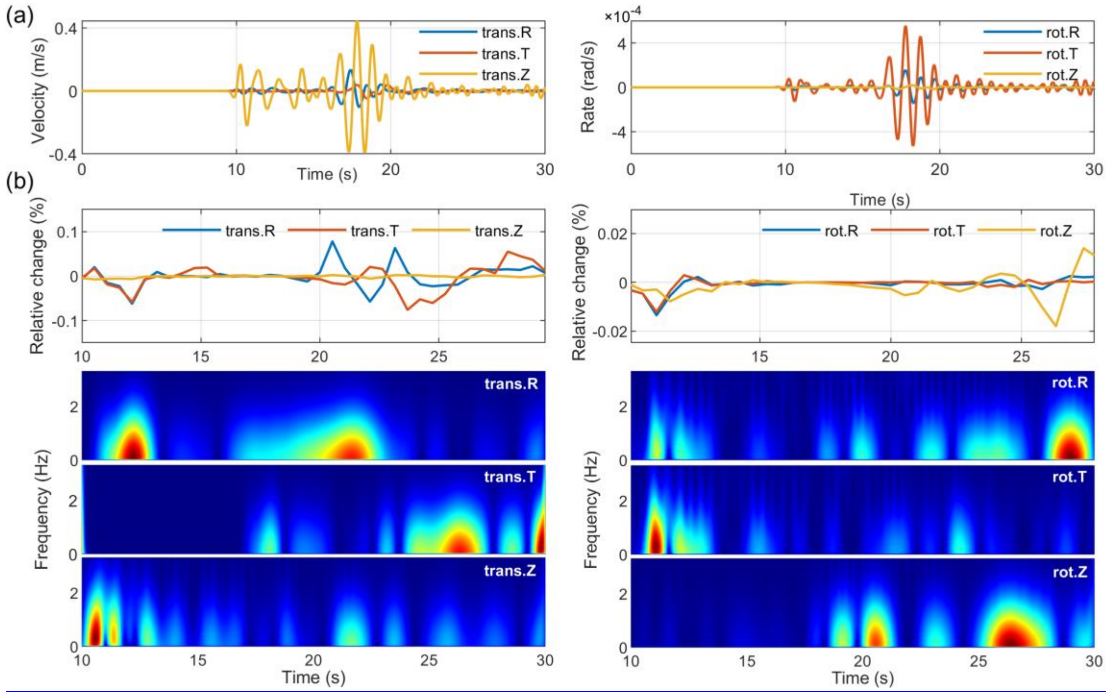

Figure 11. (a) Synthetic 6C seismic records under linear condition, and (b) relative changes in RMS amplitude and nonlinear-induced~~relative changes in RMS amplitudes and~~ time-frequency ~~spectra~~spectral difference for E1~~1 differences between linear and nonlinear conditions~~.

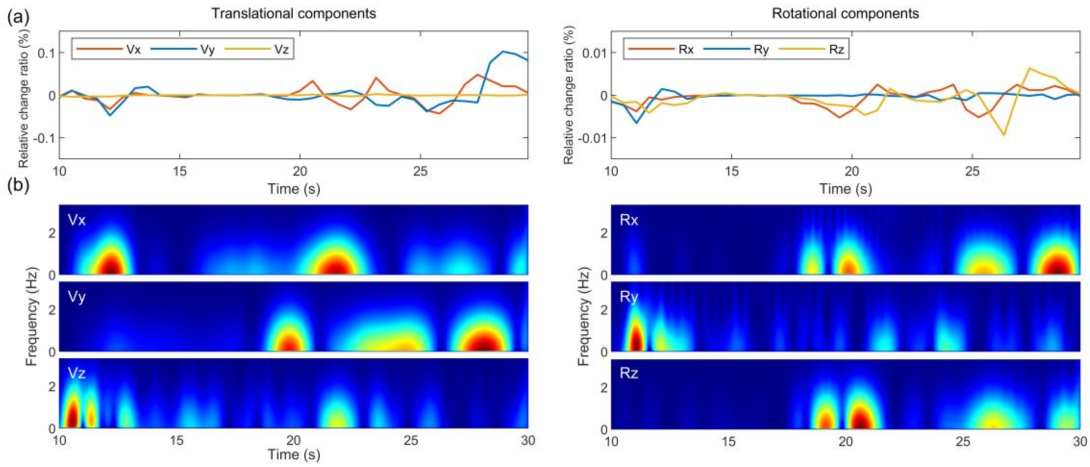

~~**Figure 10.** Relative change in RMS amplitude (a) and normalized time-frequency difference (b) of translational components (left subfigures) and rotational components~~

~~(right subfigures) between linear and nonlinear scenarios~~

~~**Table 3** Simulation parameters for E2.~~

~~Items~~	~~Parameters~~
~~Source type~~	~~Eq. (21)~~
~~Central frequency~~	~~0.5 Hz~~
~~Grid interval~~	~~5 km~~
~~Time interval~~	~~2 ms~~
~~Source location~~	~~(0, 310 km, 30 km)~~
~~Receiver location~~	~~(100, 0 km, 0 km)~~
~~Recording time~~	~~200 s~~

The larger-magnitude E2 simulation demonstrates stronger nonlinear effects, particularly in trans.Z and rot.T components (Fig. 12). Rayleigh waves show pronounced nonlinear distortions, while P-waves in trans.Z and surface waves in trans.R and T components exhibit moderate changes. S-waves and surface waves in the rot.R component are also affected, though rot.Z waveforms display minimal nonlinear alterations.

~~he trans.Z and rot.T components exhibit prominent amplitude compared to other components (Fig. 12(a)).~~

~~For simulating E2, the model is 150 km (x) ×350 km (y) × 50 km (z), and the modeling parameters are detailed in Table 3. The synthetic 6C seismic records (Fig. 11a) show a dominance of the Vz component over the Vx and Vy components, while the Rx and Ry components exhibit greater strength than the Rz component, indicating the rotational motions primarily occurring in the horizontal direction. In the actual observed records (Fig. 11b), where the seismometer is positioned on a solid rock within a tunnel, indicate a slight dominance of the Vz component over the Vx and Vy~~

~~components, while the Rz component is slightly weaker than the Rx and Ry components, which in general aligns with the relative amplitude strength of theoretical simulations. These observations suggest that the rotational motions for E2 are predominantly horizontal, and the site effect is relatively weaker. The amplitude difference between the actual observed rotational and translational components is smaller than the amplitude difference between the simulated translational and rotational components, consistent with the characteristic shown in Fig. 9.~~

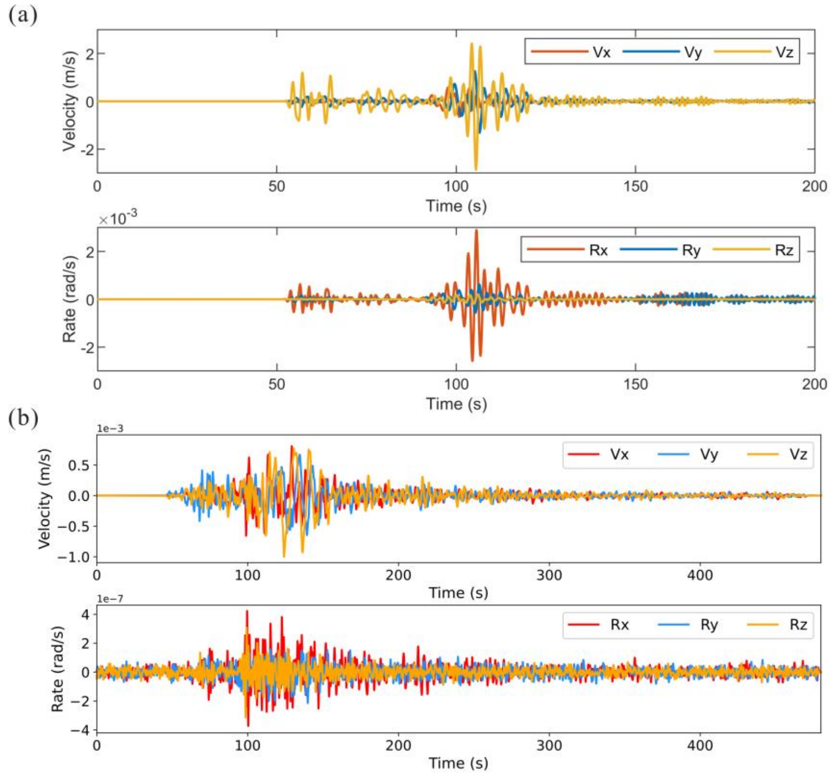

~~**Figure 11.** 6C seismic records of (a) simulation under linear small deformation and (b) actual observation for E2. In (b), a band-pass filter of 0.1 Hz to 1 Hz is applied~~

~~Fig. 12(a~~b~~) presents the root mean square (RMS) amplitudes of E2 from linear simulations, with the results incorporating nonlinearity depicted as error bars. It~~

~~shows that nonlinearity exerts more pronounced's impact is more significant effects on the translational components motions than the rotational motions, with the (generally longer error bars). The Vz trans.Z and rot.T components experiences showing a the greater influence (generally widestr amplitude error bars) among the translational componentsand the the Rx-component RMS amplitude is more affected. Fig. 12(b)the time frequency differences illustrates that both direct S waves and surface waves in both translational and rotational components are primarily affected by nonlinearity, albeit with distinct seismic phases affected within their respective frequency spectra. Additionally, the reflected waves on the Vz trans.Z component also exhibit considerable errorseffects.~~

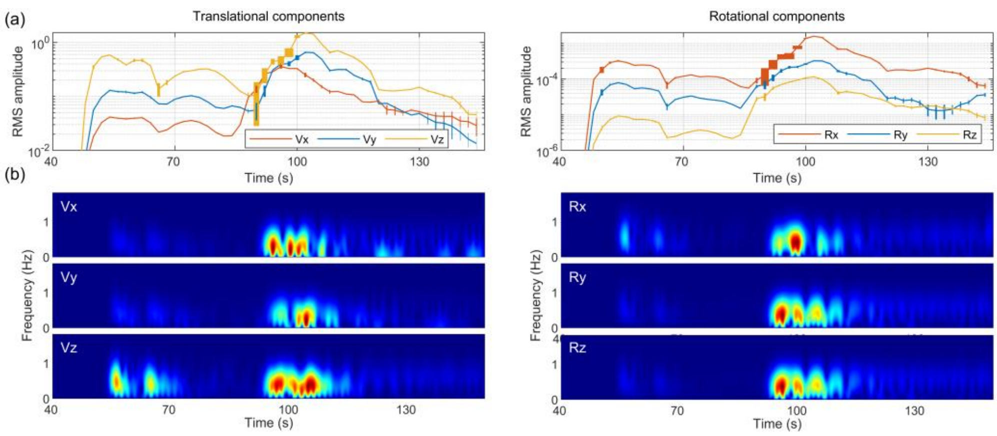

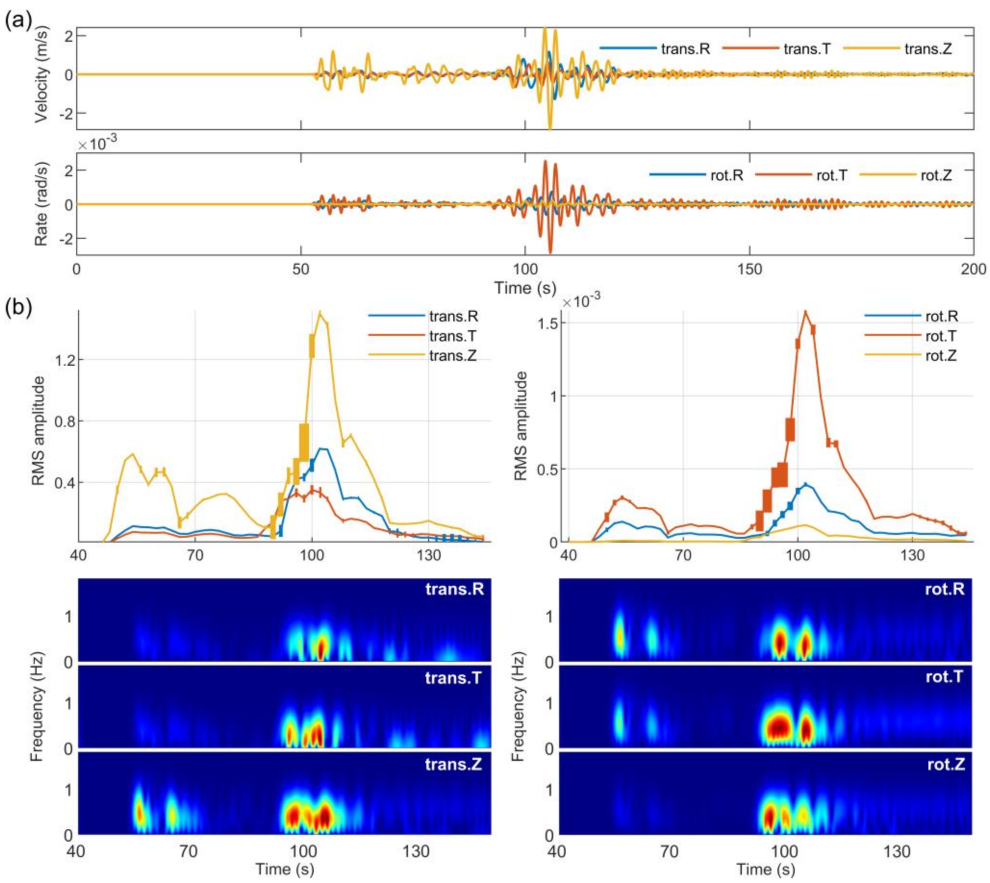

Figure 12. (a) Synthetic 6C seismic records under linear condition, and (b) RMS amplitude and nonlinear-induced time-frequency spectral difference for E2. ~~Synthetic 6C seismic records under linear condition, and (b) Relative relative changes in RMS amplitudes (a) and normalized time-frequency spectral differences (b) of translational components (left subfigures) and rotational components (right subfigures) between linear and nonlinear scenariosconditions~~

The simulations of E1 and E2 reveal some observational implications. For E1, the weak nonlinear effects (<1% amplitude changes) suggest that its receiver location may lie in a region of suppressed nonlinear coupling, likely due to unfavorable source-receiver geometry. In contrast, E2 exhibits stronger nonlinear signatures, particularly in surface waves. This enhanced nonlinear sensitivity in surface waves arises from their inherent P-S interference characteristics, making it a more viable candidate for studying nonlinear effects.

While rotational Z-component Love waves show minor nonlinear alterations, the translational R/T and rotational R/T components demonstrate more significant changes, particularly in Rayleigh waves. These findings emphasize the need to prioritize specific wave phases and components in future observational data studies. For practical applications, wavefield separation techniques may be necessary to isolate S-waves and surface waves in translational and rotational components, where nonlinear effects are most pronounced.

5 Discussion

~~In contrast to traditional wave propagation limited to linear terms, ~~T~~t~~he incorporation of Green strain tensor-based nonlinearity into classical elastodynamic theory introduces ~~is expressed as a function encompassing both the strain tensor and the rotation tensor. By incorporating nonlinear components , the elastic wave equations now incorporate third~~higher-order~~ derivatives of the~~ displacement gradient terms (Eqs. (7) and (–9)),~~field.~~ —fundamentally altering seismic wave~~These higher-order nonlinear terms significantly influence the ~~dynamics ~~properties of seismic waves,~~by coupling ~~affecting both ~~volumetric~~ changes~~ and shear deformation ~~during material deformation~~modes. In linear elasticity theory, volumetric (principal) and shear strains are completely decoupled, and P-wave and S-wave are driven by normal stresses and shear stresses, respectively.

While ISO source simulation reveals~~in nonlinear media suggests potential coupling between~~ P-~~waves and~~ S-wave~~s~~ conversion through nonlinear dilatational-shear interactions, the real-world manifestation of such phenomena is constrained by multi-~~scale~~factor geological complexities absent in our idealized models.~~actual observations reveal more intricate nonlinear effects constrained by multiple factors.~~ Future work should prioritize simulations incorporating velocity gradients and attenuation profiles to quantify how propagation paths modulate nonlinear effects, particularly for surface waves where site amplification may enhance nonlinear coupling.

The differences between E1 and E2 simulations further highlight the need to explore complex source characteristics. While E2's larger magnitude produced clearer nonlinear signatures, most natural earthquakes involve composite rupture dynamics and asymmetric moment tensors. Expanding simulations to include finite-fault sources and spatially varying rupture kinematics could reveal how source complexity interacts with nonlinear strain accumulation.

Finally, while rotational components show theoretical sensitivity to nonlinear effects, their practical utility remains constrained by observational challenges. Field rotational motions are inherently weaker than translations, and current instruments struggle to resolve most nonlinear changes. Addressing these limitations will require coordinated advances in sensor technology, wavefield separation methods, and targeted field observations focusing on moderate-strong earthquakes where nonlinear effects may cross detection thresholds.

~~However, natural exhibit far greater complexity in source and media characteristics, including diverse fault rupture processes, anisotropic medium properties, site effects and so on. Factors such as seismic source mechanism, propagation path, surface conditions exert complex and unclear influences on nonlinear effectsThese factors interact in complex ways, impacting seismic wave propagation.~~

~~Since the mechanics of seismic rotation may be related to nonlinear elasticity (Guyer and McCall, 1995; Guyer and Johnson, 1999), asymmetric moment tensor (Teisseyre et al., 2003; Teisseyre, 2010), medium heterogeneity, anisotropy (Pham et al., 2010; Sun et al., 2021), and site effects, by examining the intimate relationship between nonlinear effects and propagation path and medium characteristics, we can gain a more objective and accurate understanding of the impact of nonlinearity on seismic waves, particularly regarding rotational components.~~

6 Conclusions

This work establishes a theoretical and numerical framework for analyzing nonlinear ~~Utilizing~~ seismic wave propagation ~~equations that assume linear small deformations as a foundational framework, we have derived elastic-wave formulations incorporating~~through Green strain tensor~~'s nonlinear components~~ strain tensor ~~elastodynamic~~ formulation~~equations~~. Numerical s~~SThrough numerical s~~imulations~~ and analyses in models~~ of three fundamental seismic moment tensor sources (ISO, CLVD, DC) and two moderate-to-strong magnitude~~Taiwan coastal~~

earthquakes yield the following key conclusions.~~, to study the wavefield disparities between linear and nonlinear scenarios of both translational and rotational motions. The principal findings of our study can be summarized as follows.~~

(i) Force-source-type dependency: The spatial distribution is intrinsically tied to source kinematics. ISO sources generate overall uniform nonlinear anomalies through volumetric-shear coupling, CLVD sources amplify directional anomalies along principal strain axes of compression/expansion, and DC sources restrict localized nonlinearity to fault-aligned force couple orientations. These patterns arise from how each force source geometry interacts with the nonlinear strain tensor.~~When simulating ISO sources in media with nonlinear effects, the interaction between seismic waves leads to the generation of S-waves. For CLVD and DC sources, nonlinear effects cause the intensities of P-waves and S-waves on translational components to trend towards equilibrium, while S-waves exhibit prominence on rotational components.~~

(ii) Magnitude-energy relationship: Nonlinear effects scale exponentially with seismic moment, becoming observationally significant for magnitudes above Mw5. At Mw7, rotational components exhibit over 20% relative changes compared to linear predictions, whereas changes remain negligible for Mw <4 events. This underscores the importance of strain amplitude in triggering detectable nonlinear coupling.~~The impact of nonlinear media on seismic waves varies depending on the source model. The ISO source model is most significantly affected by nonlinear effects, while the DC source model is relatively less affected. As the source intensity increases, the change in seismic wavefield energy caused by nonlinear media exhibits an~~

~~exponential growth trend.~~

(iii) Rotational motion sensitivity: Rotational components generally demonstrate higher nonlinear sensitivity than translational components. Their practical detectability depends on source-receiver azimuth.~~In simulations of pure fundamental seismic sources, the error of linear approximation for rotation is more significant in cases of strong earthquakes, while the nonlinear effects produced by microearthquakes and small earthquakes can be ignored. The S waves and surface waves recorded by seismic rotational components have certain significance for studying the impact of nonlinearity on the propagation characteristics of seismic waves.~~

(iiii) Wave-type specificity: Surface waves exhibit stronger nonlinear signatures than body waves in both earthquake simulations, likely due to their inherent P-S interference during propagation. However, current models inadequately address surface wave nonlinearity, suggesting unresolved interactions between nonlinear effects and site amplification.

~~Rayleigh waves dominate the simplified simulations of E1 and E2, but the presence of Love waves in actual observations may be related to site effects or complex propagation media. The linear approximation error of E1 simulation is very small, while the error of E2 simulation is larger, due to differences in their magnitude and potentially the radiation azimuth of the seismic source that leads to inhomogeneous nonlinear effects.~~

Author contributions. WL: conceptualization, methodology, investigation, formal analysis, writing - original draft. YW: conceptualization, writing - original draft and revised draft. CC: investigation, formal analysis. LS: methodology.

Data availability. All data is simulated and available upon reasonable request. ~~and resourcesThe seismic records of E1 are provided by the Institute of Earth Sciences, Academia Sinica, Taiwan, China. The translational records of E2 are acquired from the Fujian Earthquake Agency~~

Competing interests. The contact author has declared that neither of the authors has any competing interests.

Disclaimer. Publisher's note: Copernicus Publications remains neutral with regard to jurisdictional claims made in the text, published maps, institutional affiliations, or any other geographical representation in this paper.

Financial support. This research is financially supported by the National Natural Science Foundation of China (No. 42150201、No. 62127815、No. U1839208).

References

Aki, K., and P. G. Richards. Quantitative seismology, 2nd ed, California: University Science Books, https://doi.org/10.1029/2003EO210008, 2002.

Bataille, K., Contreras, M.: Nonlinear elastic effects on permanent deformation due to large earthquakes, Phys. Earth Planet. Inter., 175(1), 47-52, https://doi.org/10.1016/j.pepi.2008.02.016, 2009.

~~Bernauer, F., Wassermann, J., Guattari, F., Frenois, A., Bigueur, A., Gaillot, A., de Toldi, E., Ponceau, D., Schreiber, U., and Igel, H.: BlueSeis3A: Full characterization of a 3C broadband rotational seismometer, Seismol. Res. Lett., 89(2A), 620–629, https://doi.org/10.1785/0220170143, 2018.~~

Bernauer, M., Fichtner, A., and Igel, H.: Reducing nonuniqueness in finite source inversion using rotational ground motions, J. Geophys. Res.-Solid Earth, 119(6), 4860-4875, https://doi.org/10.1002/2014JB011042, 2014.

Chen, C., Wang, Y., Sun, L. X., Lin, C. J., Wei, Y. x., Liao, C. Q., Lin, B. H.,and Qin, L. P.: Six-component earthquake synchronous observations across Taiwan Strait: Phase velocity and source location, Earth and Space Science, 10, e2023EA003040, https://doi.org/10.1029/2023EA003040, 2023.

~~Cao, Y. W., Chen, Y. J., Zhou, T., Yang, C. X., Zhu, L. X., Zhang, D. F., Cao, Y. J., Zeng, W. Y., He, D., and Li, Z. B.: The development of a new IFOG-based 3C rotational seismometer, Sensors, 21(11), 3899, https://doi.org/10.3390/s21113899, 2021.~~

Chen, Q. J., Yin, J. E., and Yang, Y. S.: Time-frequency characteristic analysis of six-degree-freedom ground motion records, Chinese Quarterly of Mechanics, 35, (3), 499-506, https://link.oversea.cnki.net/doi/10.15959/j.cnki.0254-0053.2014.03.033, 2014 (in Chinese).

Dong, L. G., and Ma, Z. T.: A staggered-grid high-order difference method of one-order elastic wave equation, Chinese J. Geophys., 43(3), 411-419, 2000 (in Chinese).

Donner, S., Bernauer, M., and Igel, H.: Inversion for seismic moment tensors combining translational and rotational ground motions, Geophys. J. Int., 207(1), 562-570, https://doi.org/10.1093/gji/ggw298, 2016.

Feng, X., Fehler, M., Brown, S., Szabo, T. L., and Burns, D.: Short-period nonlinear viscoelastic memory of rocks revealed by copropagating longitudinal acoustic waves, J. Geophys. Res.-Solid Earth, 123(5), 3993–4006, https://doi.org/10.1029/2017JB015012, 2018.

Graizer, V. M.: Strong motion recordings and residual displacements: what are we actually recording in strong motion seismology? Seismol. Res. Lett., 8(4), 635-639, https://doi.org/10.1785/gssrl.81.4.635, 2010.

Graizer, V. M.: Inertial seismometry methods, Earth Physics, 27(1), 51-61, 1991.

Graves, R. W.: Simulating seismic wave propagation in 3D elastic media using staggered-frid finite differences, Bull. Seismol. Soc. Am., 86(4), 1091-1106, 1996.

Gilbert, F.: Excitation of the normal modes of the Earth by earthquake sources, Geophys. J. R. astr. Soc, 22(2), 223-226, https://doi.org/10.1111/j.1365-246X.1971.tb03593.x, ~~2010~~1970.

~~Guyer, R. A., and McCall, K. P.: Hysteresis, discrete memory, and nonlinear wave propagation in rock: A new paradigm, Phys. Rev. Lett., 74(17), 3491-3495,~~

~~https://doi.org/10.1103/physrevlett.74.3491, 1995.~~

Guyer, R. A., and Johnson, P. A.: Nonlinear mesoscopic elasticity: evidence for a new class of materials, Physics Today, 52(4), 30-36, https://doi.org/10.1063/1.882648, 1999.

Hua, S. B., and Zhang, Y.: Numerical experiments of moment tensor inversion with rotational ground motions, Chinese J. Geophys., 65(1), 197-213, https://doi.org/10.6038/cjg2022P0668, 2022 (in Chinese).

Huras, L., Zembaty, Z., Bonkowski, P. A., and Bobraet, P.: Quantifying local stiffness loss in beams using rotation rate sensors, Mech. Syst. Signal Proc., 151, 107396, https://doi.org/10.1016/j.ymssp.2020.107396, 2021.

Ichinose, G. A., Ford, S. R., and Mellors, R. J.: Regional moment tensor inversion using rotational observations, J. Geophys. Res.-Solid Earth, 126(2), e2020JB020827, https://doi.org/10.1029/2020JB020827, 2021.

Jia, L., Yan, S. G., Zhang, B. X., and Huang, J.: Research on perturbation method for nonlinear elastic waves, J. Acoust. Soc. Am., 148, EL289–EL294, https://doi.org/10.1121/10.0001980, 2020.

Jost, M. L., and Hermann, R. B.: A students guide to and review of moment tensors, Seism. Res. Lett., 60, 37-57, https://doi.org/10.1785/gssrl.60.2.37, 1989.

Knopoff, L., and Randall M. J.: The compensated linear-vector dipole: A possible mechanism for deep earthquakes, J. Geophy. Res., 75(26), 4957–4963, https://doi.org/10.1029/JB075i026p04957, 1970.

Kozak, J. T.: Tutorial on earthquake rotational effects: historical examples, Bull.

Seismol. Soc. Am., 99(2B), 998-1010, https://doi.org/10.1785/0120080308, 2009.

~~Lai, X. L., and Sun, Y.: Three component rotational ground motion obtained from explosive source data, Earth science, 42(4), 645—651, 2017 (in Chinese).~~

Laske, G., Masters, G., Ma, Z. T., and Pasyanos, M.: Update on CRUST1. 0-A 1-degree global model of Earth's crust, EGU General Assembly 2013, 15, EGU2013-2658, 2013.

Lee, C. E. B., Celebi, M., Todorovska, M. I., and Diggles, M. F.: Rotational seismology and engineering applications — Proceedings for the First International Workshop, Menlo Park, California, U.S.A.—September 18 to 19, 2007: U.S. Geological Survey Open-File Report 2007-1144, 46 p. http://pubs.usgs.gov/of/2007/1144/, 2007.

Li, H. N.: Study on rotational components of ground motion, Journal of Shenyang Architectural and Civil Engineering Institute, 7(1), 88-93, 1991 (in Chinese).

Li, H. N., and Sun, L. Y.: Rotational components of earthquake ground motions derived from surface waves, Earthq. Eng. Eng. Vib., 21(1), 15-23, https://link.oversea.cnki.net/doi/10.13197/j.eeev.2001.01.003, 2001 (in Chinese).

Madariaga, R.: Dynamics of an expanding circular fault, Bull. Seismol. Soc. Am., 66(3), 639-666, https://doi.org/10.1007/BF02246368, 1976.

McCall, K. R.: Theoretical study of nonlinear elastic wave propagation, J. Geophys. Res., 99(B2), 2591-2600, https://doi.org/10.1029/93JB02974, 1994.

Moczo, P., Robertsson, O. J., and Eisner, L.:The finite-difference time-domain method for modeling of seismic wave propagation, Advances in Geophysics, 48, 421-516. https://doi.org/10.1016/S0065-2687(06)48008-0, 2007.

Oliveira, C. S., and Bolt, B. A.: Rotational components of surface strong ground motion, Earthq. Eng. Struct. D. 18(4), 517–526, https://doi.org/10.1002/eqe.4290180406, 1989.

Pei, Z. L.: Numerical simulation of elastic wave equation in 3-D anisotropic media with staggered-grid high-order difference method, Geophysical Prospecting for Petroleum, 44(4), 308-315, https://doi.org/10.3969/j.issn.1000-1441.2005.04.002, 2005 (in Chinese).

~~Pham, N. D., Igel, H., Puente, J. D. L., Käser, M., and Schoenberg, M. A.: Rotational motions in homogeneous anisotropic elastic media, Geophysics 75(55), D47-D56, https://doi.org/10.1190/1.3479489, 2010.~~

Renaud, G., Le Bas, P. Y., and Johnson, P. A.: Revealing highly complex elastic nonlinear (anelastic) behavior of Earth materials applying a new probe: Dynamic acoustoelastic testing, J, Geophys. Res.-Solid Earth, 117, B06202, , https://doi.org/10.1029/2011JB009127, 2012.

Renaud, G., Rivière, J., Le Bas, P. Y., and Johnson, P. A.: Hysteretic nonlinear elasticity of Berea sandstone at low-vibrational strain revealed by dynamic acoustoelastic testing, Geophys. Res. Lett., 40(4), 715-719, https://doi.org/10.1002/grl.50150, 2013.

Sun, L., Yu, Y., Lin, J. Q., and Liu, J. L.: Study on seismic rotation effect of simply supported skew girder bridge, Earthquake Engineering and Engineering Dynamics, 37(4), 121-128, https://doi.org/10.13197/j.eeev.2017.04.121.sunl.014, 2017 (in Chinese).

~~Sun, L. X., Wang, Y., Li, W., and Wei, Y. X.: The characteristics of seismic rotations in VTI medium, Appl. Sci-Basel, 11(22), 10845, https://doi.org/10.3390/app112210845, 2021.~~

Sun, L. X., Zhang, Z., and Wang, Y.: Six-component elastic-wave simulation and analysis, EGU General Assembly 2018, Geophysical Research Abstracts, 20, EGU2018-14930-1, 2018.

~~Teisseyre, R., Suchcicki, J., Teisseyre, K. P., Wiszniowski J., and Palangio, P.: Seismic rotation waves: Basic elements of the theory and recordings, Annals of Geophysics, 46(4), 671–685, https://doi.org/10.4401/ag-4375, 2003.~~

~~Teisseyre, R.: Tutorial on new developments in the physics of rotational motions, Translated World Seismology, 99(2A), 1028-1039, https://doi.org/10.1785/0120080089, 2010.~~

TenCate, J. A., Malcolm, A. E., Feng, X., and Fehler, M. C.: The effect of crack orientation on the nonlinear interaction of a P wave with an S wave, Geophys. Res. Lett., 43(12), 6146-6152, https://doi.org/10.1002/2016GL069219, 2016.

Virieux, J.: P-SV wave propagation in heterogeneous media; velocity-stress finite-difference method, Geophysics, 51(4), 889-901, https://doi.org/10.1190/1.1442147, 1986.

Wang, L., Luo, Y. H., and Xu, Y. H.: Numerical investigation of Rayleigh-wave propagation on topography surface, J. Appl. Geophys., 86, 88–97, https://doi.org/10.1016/j.jappgeo.2012.08.001, 2012.

~~Wang, X. S., and Lv, J.: The holistic clockwise rotation possibly existed in Taiwan region - in addition on the seismicity feature and earthquake prediction in its adjacent areas, South China Journal of Seismology, 2, 48-54, https://doi.org/10.3969/j.issn.1001-8662.2006.02.008, 2006 (in Chinese).~~

Wessel, P., Luis, J. F., Uieda, L., Scharroo, R., Wobbe, F., Smith, W. H. F., and Tian, D.: The generic mapping tools version 6, Geochemistry, Geophysics, Geosystems, 20, 5556–5564, https://doi.org/10.1029/2019GC008515, 2019.

Xu, Y. X., Xia, J. H., and Miller, R. D.: Numerical investigation of implementation of airearth boundary by acoustic-elastic boundary approach, Geophysics, 72 (5), SM147–SM153, https://doi.org/10.1190/1.2753831, 2007.

Yan, Y. Y.: Seismic response analysis of high-rise building under different types of multi-dimensional earthquake ground motions (Ph.D. dissertation), Jiangsu University, 2017(in Chinese).

Yu, S. B., Kuo, L. C., and Punongbayan, R. S., Emmanuel, G.R.: GPS observation of crustal deformation in Taiwan-Luzon region, Geophys. Res. Lett., 26(7), 923-926, https://doi.org/10.1029/1999GL900148, 1999.

Yang, D. H., Liu, E., Zhang, Z.J., and Teng, J.: Finite-difference modelling in two-dimensional anisotropic media using a flux-corrected transport technique, Geophys. J. Int., 148(2), 320–328, https://doi.org/10.1046/j.0956-540x.2001.01575.x, 2002.

~~Zhao, K. C., and Zhang, X. B.: Distinguishing underground nuclear test by matrix~~

~~decomposition, Acta Scientiarum Naturalium Universitatis Pekinensis, 58(4), 609-614, https://link.oversea.cnki.net/doi/10.13209/j.0479-8023.2022.042, 2022 (in Chinese).~~

Zheng, H. S., Z. J. Zhang, and Liu, E. R.: Nonlinear seismic wave propagation in anisotropic media using the flux-corrected transport technique, Geophys. J. Int., 165(3), 943-956, https://doi.org/10.1111/j.1365-246X.2006.02966.x, 2006.

~~Zheng, X.,F., Cheng, Z.,H., and Zhang, C. H.: The development of seismic monitoring in Taiwan, Seismological and Geomagnetic Observation and Research, 26(3), 100-107, https://doi.org/10.3969/j.issn.1003-3246.2005.03.017, 2005 (in Chinese).~~

Zhou, C., Zeng, X. Z., Wang, Q. L., and Liu, W. Y., and Wang, C. Z.: Rotational motions of the Ms7.0 Jiuzhaigou earthquake with ground tilt data, Science China Earth Science, 62(5), 832-842, https://doi.org/10.1007/s11430-018-9320-3, 2019.